

1 **Hadean-aged felsic sediments recycled through the deep mantle by early plate tectonics**

2

3 Bradley J. Peters¹, Marc C. Halfar¹, Courtney J. Rundhaug^{1,2}, Paterno Castillo³, Maria
4 Schönbacher¹

5

6

7 ¹Institute of Geochemistry and Petrology, ETH Zürich, 8092 Zürich, Switzerland

8 ²Centre for Star and Planet Formation, University of Copenhagen, 1350 Copenhagen,
9 Denmark

10 ³Scripps Institution of Oceanography, University of California San Diego, La Jolla, CA
11 92093-0244, United States

12

13 Abstract word count: 269

14 Main text word count: 2896

15 Figures: 4

16

17 Supplementary text, figures, and tables accompany this article.

18

19 *This is a non-peer reviewed preprint submitted to EarthArXiv and under review at Science*
20 *Advances.*

21

22 **One sentence summary:** The Marquesas volcanic hotspot contains a four-billion-year-old
23 geochemical record of deep subduction of felsic sedimentary materials, implying that Earth's
24 pathway to habitability through plate tectonics began very early in its history.

25 **Abstract**

26 The unresolved question of when modern tectonic processes arose on Earth has restricted our
27 understanding of how and how quickly Earth reached its present, habitable form. Plate
28 tectonics, and in particular deep subduction, is central to many facets of habitability: it controls
29 heat flow, biogeochemical cycling, and creates a variety of marine and terrestrial biomes that
30 are crucial for biological evolution. Many petrological, geodynamical, and geochemical
31 perspectives have offered circumstantial evidence for both an early onset of plate tectonics, in
32 the first 10% of Earth's history, or a late onset after the great oxidation event (2.5 Ga ago). We
33 present geochemical evidence from the products of early subduction, which have been recycled
34 into the deep mantle and then tapped by the modern Marquesas volcanic hotspot. These
35 products must have been stored and protected in the deep mantle largely unchanged for more
36 than four billion years before they were brought to the surface by the Marquesas mantle plume.
37 The felsic composition of these subducted materials further requires that both subcrustal
38 melting and sedimentation processes were active in some form before this time. The early
39 development of a mature plate tectonic system on Earth implies that its pathway to complex life
40 was protracted: the foundations for habitability potentially began billions of years before the
41 emergence of life. Emerging planetary bodies may, therefore, need long-term sustained plate
42 tectonic processes to become host to complex biological systems. Further, the preservation of
43 evidence for foundational planetary events in geologically young rocks, rather than ancient
44 rocks, reveals that Earth's volcanic hotspots could provide a defining perspective on the early
45 planetary-scale processes that build Earth-like planets.

46 **Introduction**

47 Although the earliest part of Earth's geological history established the conditions
48 required for habitability, the geological record from this period has been almost entirely lost.
49 One central question about the Earth's earliest history is when it became habitable, which is in
50 turn related to the initiation of deep biogeochemical cycles and climate stability through plate
51 tectonics [1]. Subduction is accepted as a key element of plate tectonics, since it requires that
52 sections of the lithosphere experienced mechanical strengthening, forming 'plates' that can
53 coherently sink (subduct) in the mantle. While deep subduction (continuing at least to the
54 mantle transition zone, i.e. >400 km deep) is understood to be a mostly self-sustaining process
55 due to the pulling mechanism of subduction, it remains unclear how and when deep subduction
56 initiated on Earth [2] and whether Archean tectonic regimes were characterized by shallow,
57 rather than deep subduction [3].

58 There is broad agreement that the generation of felsic rocks on the early Earth is
59 evidence that pre-existing mafic rocks were re-melted after being transported to subcrustal
60 depths, possibly, although not necessarily by subduction [4]. Circumstantial evidence for the
61 existence of early felsic crust, derived from its remaining mineral components [5, 6] or the
62 residual composition of the mantle left behind during crustal building [7, 8], implies that felsic
63 continental plates were already being built as far back as 4.4 Ga ago. However, although the
64 production of ancient felsic crust requires that mafic crust is buried and heated, the most
65 common type of Archean felsic rock does not unambiguously require deep subduction similar
66 to plate boundary processes observed today [9, 10]. Instead, there remains debate over whether
67 subduction is required to build felsic crust [3, 6, 9], or whether subduction tectonics would even
68 initially work against the stability of mature felsic crust [11].

69 The scarcity of Archean-aged rock representatives for subduction, such as ophiolites or
70 high-pressure metamorphic rocks [12, 13], precludes direct study of subduction initiation in the
71 early rock record. The preservation of Archean-aged orogenic rock assemblages has been used
72 to infer an early onset of subduction [14], but neither documents subduction itself nor permits
73 a direct comparison of potential Archean subduction to modern plate tectonics. Some
74 petrological and geodynamical models have favored an early start of tectonic subduction (e.g.,
75 [6, 15]), but without primary evidence from the products of this subduction. A complementary
76 perspective to studies of Archean-aged rocks is provided by Earth's volcanic hotspots, some of
77 which have a geochemical memory that spans more than 4.5 billion years [16-18], which is
78 longer than the longest lifespan of rocks on Earth's surface [19]. Volcanic hotspots are known
79 to tap subducted materials from the deep mantle [20], which may have been stored there for

80 long geological timescales (≥ 2.5 Ga) [21] and may therefore preserve information about early
81 tectonic processes. We present geochemical evidence from the Marquesas volcanic hotspot
82 (southern Pacific Ocean) that subduction like that observed in modern plate tectonics was
83 already active by the end of the Hadean Eon (ca. 4 Ga ago) and that it involved felsic geological
84 materials akin to modern continental crust. Therefore, deep geochemical cycles critical to life
85 on the modern Earth may have been established very early in Earth's history.

86

87 **Mantle plumes as conduits for ancient geochemical signals**

88 Many volcanic hotspots, like the Marquesas archipelago, are underlain by plumes that
89 extend into the deep mantle [22]. The bases of many mantle plumes are associated with
90 seismically anomalous domains in the deep mantle known as large low shear-wave velocity
91 provinces (LLSVP), like the Pacific LLSVP under the Marquesas Islands. These LLSVP are
92 commonly thought to represent stable thermochemical piles that may originate as dense
93 primitive or subducted materials that accumulated at the base of the mantle [23-25]. The
94 association of these components leads to the joint tapping of primitive and subducted materials
95 by volcanic hotspots in a process known as tectonic recycling [24]. In many hotspot sources,
96 the subducted material represents altered oceanic crust, oceanic mantle lithosphere, and/or the
97 overlying sediment associated with oceanic crust (e.g., [26]). In a few locations, including the
98 Marquesas, the erupted lavas represent multiple subducted and primitive components with
99 distinct geochemical compositions that were mixed with each other before or during mantle
100 melting (**Figure 1**) [27]. The distribution of these components has a clear geographical structure
101 sometimes referred to as compositional "stripes" that divide the various islands or eruptions
102 into groups with distinct origins in the deep mantle [27]. The geochemical compositions
103 exhibited by the components found in the Marquesas are not present in upper mantle-derived
104 rocks, and the lack of a geochemically depleted upper mantle component in Marquesas hotspot
105 lavas strongly implies that their parental magmas are instead dominated by recycled, deep
106 mantle components [27, 28].

107 The Marquesas hotspot is geochemically unique among global hotspots in that it appears
108 to represent at least two mixing trends that each involve primitive material and either recycled
109 oceanic crust (termed 'high- μ ' or HIMU for its relatively high time-integrated $^{238}\text{U}/^{204}\text{Pb}$
110 signature) or subducted sediment (termed 'enriched mantle' or EM). It is commonly argued that
111 the diverse geochemical signatures of EM-type hotspots (e.g., Pitcairn, Hawai'i, Kerguelen,
112 Samoa) represent an array of sedimentary origins, each of which may have a distinct origin or
113 history [29]. However, the Marquesas hotspot does not display the extreme isotopic signatures

114 represented by other volcanic hotspots with HIMU (e.g., Mangaia) or EM (e.g., Samoa)
115 componentry (**Figure 1**). The relatively diluted representation of these geochemical
116 components in Marquesas lavas exacerbates the challenge of tracing the provenance of each
117 component using long-lived radiogenic isotope systems (e.g., ^{87}Rb - ^{87}Sr , ^{147}Sm - ^{144}Nd , or ^{238}U -
118 ^{204}Pb) because the unique isotopic signatures are dampened by this dilution, affecting not only
119 the isotopic signatures directly but also indirectly by altering their parent-daughter ratios.

120 The use of short-lived radiogenic systems, for which radioactive decay is restricted to
121 the Hadean Eon (≥ 4 Ga old, i.e. the first ca. 10% of Earth's history) and thus long before such
122 dilution, may simplify this issue by offering a binary perspective on the components of the
123 Marquesas mantle source: heterogeneous short-lived radiogenic isotope signatures require
124 incorporation of components with diverse Hadean-aged provenance, while homogeneous
125 signatures do not require distinct Hadean-aged sources. The presence of ancient recycled
126 materials in the Marquesas mantle source may have precluded the detection of heterogeneity in
127 the short-lived ^{182}Hf - ^{182}W radiogenic system [30], which has both lithophile (i.e. silicate-
128 loving) and siderophile (i.e. metal-loving) properties. However, the exclusively lithophile
129 nature of both Sm and Nd renders the short-lived ^{146}Sm - ^{142}Nd system ($t_{1/2} = 103$ Ma, [31]) more
130 suitable for detecting Hadean-aged geochemical signatures in the Marquesas hotspot, since both
131 its recycled and primitive components were formed through differentiation of silicate materials.
132 Thus, if any of the geochemical components of the Marquesas hotspot were originally formed
133 in the Hadean Eon, they may display heterogeneous $^{142}\text{Nd}/^{144}\text{Nd}$ ratios that can be measured
134 with high-precision analysis techniques.

135

136 **Distinct Hadean heritages for the Marquesas compositional components**

137 Like the long-lived radiogenic signatures of Marquesas basalts, their $\mu^{142}\text{Nd}$
138 ($^{142}\text{Nd}/^{144}\text{Nd}$ ratio normalized to the terrestrial standard, JNdi-1 [32], in parts per million)
139 compositions reflect a geochemically heterogeneous source (**Figure 2**). Their $\mu^{142}\text{Nd}$ signatures
140 range from -2.3 to +2.6 and reflect statistically significant heterogeneity (Supplementary
141 Information). However, if the samples are divided into groups representing their geochemical
142 componentry (**Figure 1**; Supplementary Information), each group instead reflects statistically
143 homogeneous $\mu^{142}\text{Nd}$ compositions (**Figure 2**). Samples with EM-type isotopic compositions
144 (hereafter the “EM group”; see Supplementary Information for a discussion of grouping)
145 display $\mu^{142}\text{Nd} = +2.3 \pm 1.3$ (reported uncertainties always represent 95% confidence intervals
146 calculated using Isoplot [33]; MSWD: 0.1, probability of fit: 0.87, $n = 3$), and those in the ‘focal
147 zone’ (FOZO) and HIMU groups have combined $\mu^{142}\text{Nd} = -0.8 \pm 1.2$ (MSWD: 0.6, probability

148 of fit: $0.76, n = 7$). Intensive measurement replication permits an overall uncertainty of less than
149 2 ppm for each sample group even with an estimated reproducibility of any single measurement
150 of typically ca. 5 ppm (Supplementary Information). Further, the results represent data for
151 replicate sample dissolutions processed through diverse chemical separation methods, thus
152 improving their overall reliability (Supplementary Information). The EM group and the
153 combined FOZO/HIMU groups pass a t-test for statistical distinctness (two-tailed $P = 0.004$).
154 It is also notable that the two sample groups that represent recycled materials (HIMU, $\mu^{142}\text{Nd}$
155 $= -0.7 \pm 1.4$, and EM, $\mu^{142}\text{Nd} = +2.3 \pm 1.3$) have statistically distinct $\mu^{142}\text{Nd}$ compositions,
156 meaning that the geological evolution of these deep mantle components must have diverged in
157 the Hadean Eon, and that LLSVP may contain materials with diverse Hadean histories. On the
158 other hand, the Marquesas HIMU and FOZO groups have average $\mu^{142}\text{Nd}$ values that overlap
159 within uncertainty, implying that their geological histories diverged only after the Hadean Eon.

160 Consistent with this inter-group heterogeneity, the $\mu^{142}\text{Nd}$ compositions of Marquesas
161 lavas are correlated with their $^{87}\text{Sr}/^{86}\text{Sr}$ and $^{143}\text{Nd}/^{144}\text{Nd}$, and Ce/Pb ratios, and display a more
162 complex, but interpretable relationship with their $^{206}\text{Pb}/^{204}\text{Pb}$ ratios (**Figures 3, S1**;
163 Supplementary Information). This is the first time such a correlation between $\mu^{142}\text{Nd}$ and long-
164 lived radiogenic isotopes or trace element ratios for geologically young rocks has been
165 observed. There is no statistically significant correlation between $\mu^{142}\text{Nd}$ data and the
166 siderophile W and Os isotopic systems (**Figure S1**, cf., [30]). The negative correlation between
167 $\mu^{142}\text{Nd}$ and $\epsilon^{143}\text{Nd}$ compositions requires that this relationship is not chronological, but instead
168 reflects variable mixing of an EM-like component with high $^{87}\text{Sr}/^{86}\text{Sr}$, low $\epsilon^{143}\text{Nd}$, and elevated
169 $\mu^{142}\text{Nd}$ into the Marquesas mantle source.

170

171 **The Hadean heritage of EM-type Marquesan lavas**

172 The heterogeneous $\mu^{142}\text{Nd}$ signatures of the EM and FOZO/HIMU sample groups
173 represent variable influence from at least one component that formed before the end of the
174 Hadean Eon. This component was then subjected to later dilution with a mantle component
175 possessing a $\mu^{142}\text{Nd}$ composition close to the presumed bulk Earth value ($\mu^{142}\text{Nd} \equiv 0$). The
176 combined effect of this dilution on both $\mu^{142}\text{Nd}$ and the long-lived radiogenic isotope signatures
177 of Marquesas lavas is most visible for the EM group of samples. The Marquesas EM group
178 displays a maximum $^{87}\text{Sr}/^{86}\text{Sr}$ ratio of ca. 0.7054 and $\mu^{142}\text{Nd}$ up to +2.6, whereas the HIMU and
179 FOZO groups have lower $^{87}\text{Sr}/^{86}\text{Sr}$ ratios and $\mu^{142}\text{Nd}$ very close to the bulk Earth (**Figures 3,**
180 **S1**). The effect of diluting a FOZO-like component with an EM component on $\mu^{142}\text{Nd}$ can be
181 predicted by calculating a Sr- ^{143}Nd isotopic mixing line between idealized FOZO and EM

182 components, and then projecting this line through the maximum $\mu^{142}\text{Nd}$ composition of the EM
183 group and the average $\mu^{142}\text{Nd}$ composition of the Marquesas FOZO group ($\mu^{142}\text{Nd} = -1.0 \pm 2.2$).
184 The Samoa hotspot, which overlaps and extends the Sr-Nd-Pb isotopic composition of
185 Marquesas lavas toward an EM endmember composition (**Figure 1, S2**) can be utilized as an
186 idealized EM endmember [34]. Due to the very radiogenic $^{87}\text{Sr}/^{86}\text{Sr}$ and unradiogenic $\epsilon^{143}\text{Nd}$
187 signatures of Samoan lavas, the Samoa EM endmember has been interpreted to represent
188 subducted sediments derived from felsic continental crust, which shares these isotopic
189 properties [34]. Importantly, the heritage of the Marquesas EM component need not be identical
190 to that of Samoa in order for them to approximately share an endmember Sr- ^{143}Nd -Pb isotopic
191 composition (cf., [29]). Their respective EM endmember components may instead share a Sr-
192 ^{143}Nd -Pb isotopic composition while having distinct $\mu^{142}\text{Nd}$ signatures, as is common
193 throughout the Archean record of felsic crust (e.g., [35]; see also Supplementary Information)

194 The compositional overlap between Marquesas and Samoa lavas is strong
195 circumstantial evidence that they each have an endmember source component with an isotopic
196 composition similar to recycled felsic continental crust. It is unlikely that the most extreme
197 compositions of Marquesas lavas instead represent their own endmember composition for
198 several reasons. First, most felsic continental crust is Precambrian (>0.5 Ga old), and thus has
199 Sr- ^{143}Nd -Pb isotopic compositions that are more radiogenic than the most radiogenic
200 Marquesas samples [36]. Second, if Marquesas samples with the most extreme Sr- ^{143}Nd -Pb
201 isotopic compositions were direct representatives of recycled crustal materials and thus
202 represented an endmember composition, this would likely be expressed more clearly in their
203 major and trace element compositions. For example, they would likely be relatively silicic,
204 display negative Nb anomalies and relative enrichments in U, Th, and Pb. These characteristics
205 are not observed in any Marquesas lavas (e.g., [27]), but are observed in Samoan lavas with
206 isotopic compositions close to their assumed EM endmember [34]. Finally, all Marquesas EM
207 group samples have $^3\text{He}/^4\text{He}$ ratios close to MORB [37], whereas tectonically recycled
208 materials are expected to have lower $^3\text{He}/^4\text{He}$ ratios because He is preferentially lost during
209 subduction compared to U and Th, the radiogenic parents of ^4He (e.g., **Figure 1c-1d**; [38]).
210 Thus, it is most likely that the Marquesas EM samples represent a relatively diluted EM
211 endmember deriving from recycled felsic crust.

212 Utilizing the isotopic compositions of the most extreme EM sample of [34] (cf., [39])
213 and trace element abundances of Archean-aged crust compiled from the GEOROC database
214 (Supplementary Information), the Marquesas EM group represents a ca. 0.6% contribution of a
215 Samoan EM endmember with $\mu^{142}\text{Nd}$ of $+24^{+10}_{.5}$ (**Figures 3, S3-S4**; see Supplementary

216 Information for model details). This mixing proportion compares favorably with the Marquesas
217 EM mixing models of [28] and [30]. Data for Earth's oldest rocks (up to 4 Ga old) approach
218 this $\mu^{142}\text{Nd}$ compositions suggested by the mixing models, with a maximum recorded $\mu^{142}\text{Nd}$
219 value of +20 in a 3.85 Ga-old rock [40-43]. Convective mixing quickly homogenized highly
220 positive $\mu^{142}\text{Nd}$ signatures in Earth's mantle [44], such that the cumulative average of published
221 data with positive $\mu^{142}\text{Nd}$ signatures is $<+10$ by 3.7 Ga (**Figure 4**) [45]. This value is subject to
222 significant preservation and experimental bias, but clearly indicates that the probability of
223 subducting felsic crust with average $\mu^{142}\text{Nd} \geq +20$ decreases drastically the longer the residence
224 time of that crust at the surface $\mu^{142}\text{Nd}$. If Hadean-aged felsic remains on the surface for 1-2 Ga
225 before being subducted then new felsic material, which most likely has a lower $\mu^{142}\text{Nd}$
226 signature, would be added to this crust. Thus, subduction of stochastically eroded continental
227 crust at e.g. 2.5 Ga would produce an EM endmember with $\mu^{142}\text{Nd} < +0.5$. According to the
228 current record, only subduction of felsic crust at least as old as the present rock record (4 Ga)
229 would likely produce the EM endmember required by the Marquesas $\mu^{142}\text{Nd}$ signature (i.e.,
230 $\geq +20$). Thus, the Marquesas lavas most likely tap felsic crustal material that was subducted at
231 or before 4 Ga ago without long-term storage of this crustal material at Earth's surface. The
232 presence of sufficient felsic crustal material on Earth's surface by 4 Ga ago supports very early
233 formation of felsic crust [5] and implies that tectonics in some form had been active for some
234 time before 4 Ga.

235

236 **A Hadean start for deep tectonic subduction**

237 Our Nd isotopic data require that the Marquesas mantle plume taps a tectonically
238 recycled component with a $\mu^{142}\text{Nd}$ signature at least as ancient as that found in Earth's oldest
239 crustal rocks. This necessitates that tectonic subduction was not only active, but that subducted
240 materials were transported deep enough into Earth's mantle that their compositions were
241 preserved for billions of years, precluding models such as drip subduction, sagduction, or flat
242 subduction (e.g., [46]). According to geodynamic models, the long-term preservation of
243 heterogeneous isotopic domains in Earth's mantle is only likely in the deep mantle, and most
244 probable within stable deep mantle structures [21]. This implies that the Hadean-aged
245 subduction that locked the $\mu^{142}\text{Nd}$ composition of the Marquesas EM endmember in the mantle
246 was steep and did not result in stagnation of the subducting slab in the mantle transition zone,
247 as envisaged by many models of ancient subducted crust [46, 47]. Since EM-like Sr-Nd-Pb
248 isotopic compositions like those found in the Marquesas or Samoa are unknown among upper
249 mantle-derived rocks [20], it is unlikely that the Marquesas mantle plume inherited its EM

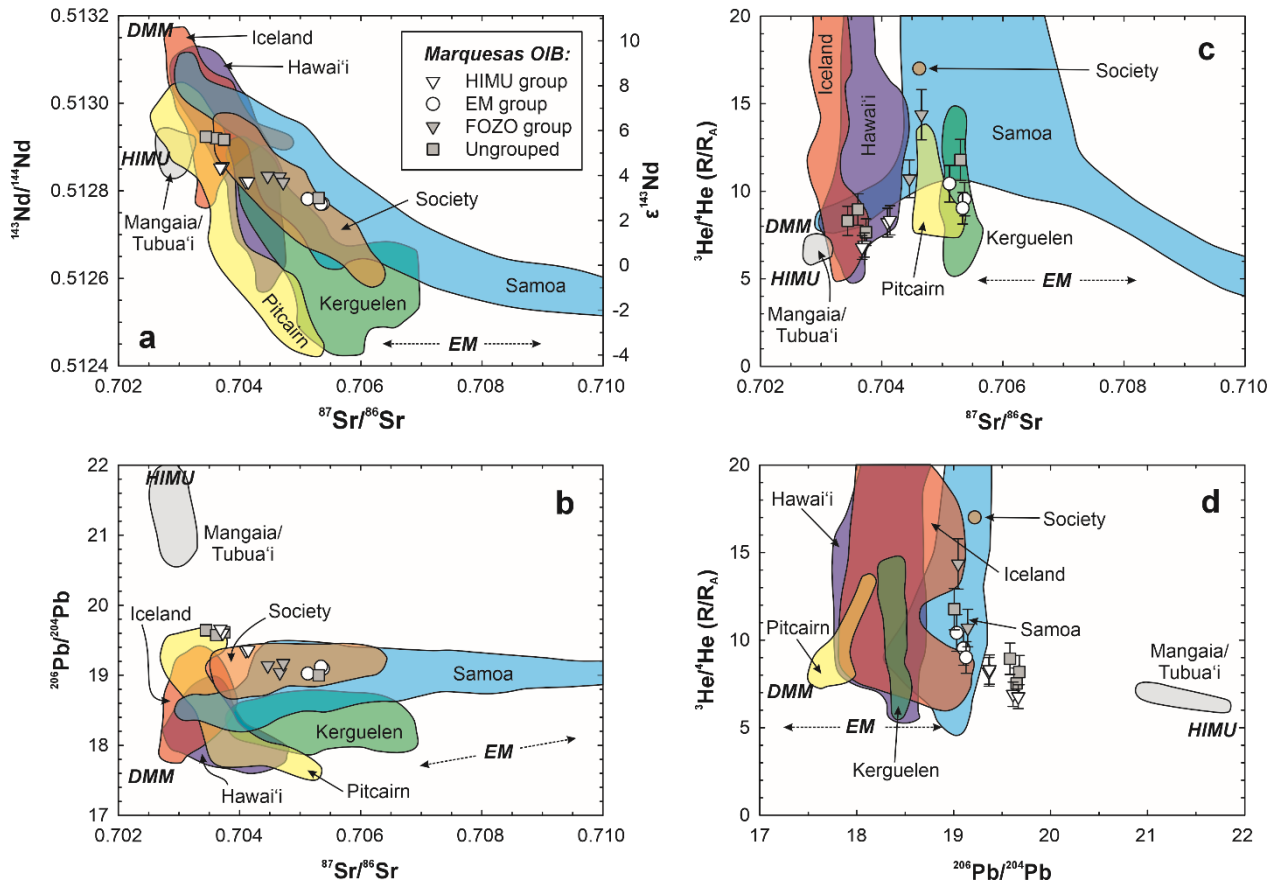
250 component from the upper mantle. Further, the strong preservation bias present in all materials
251 from the early Earth implies that the Marquesas EM component is not unique: rather, it likely
252 represents part of a larger recycled domain reflecting widespread Hadean subduction, only
253 some of which survived to the present day.

254 The operation of deep tectonic subduction by the end of the Hadean Eon strongly
255 implies that the foundation for biogeochemical cycles critical for life was laid very early in
256 Earth's history. Moreover, the subduction of sediments is often envisaged analogously to
257 modern tectonic-erosional cycles and may require that continental erosion systems were also
258 active on the early Earth (cf. the banded iron formation record, e.g., [48]). An early start to plate
259 tectonics and a long evolutionary pathway to complex life on Earth places an important
260 constraint on the search for Earth-like exoplanets as remote sensing and numerical simulation
261 techniques improve. Given the long temporal gap between the emergence of terrestrial plate
262 tectonics (≥ 4 Ga ago as proposed here) and the emergence of eukaryotic life (≥ 1.7 Ga [49]),
263 young exoplanets without emerging plate tectonic processes may be much less likely to
264 eventually host life. On the other hand, early development of plate tectonics is not a guarantee
265 that a planet will eventually generate a biosphere [50, 51]. Additional high-precision study of
266 the Hadean geochemical record preserved in subducted materials tapped by volcanic hotspots
267 may provide a more detailed record of the early evolution of Earth's tectonic landscape. EM-
268 type hotspots, in particular, are all geochemically unique, and the EM mantle component is
269 increasingly recognized as representing diverse and independent geological heritages [36],
270 some of which may have a geochemical history stretching back to the earliest Earth.

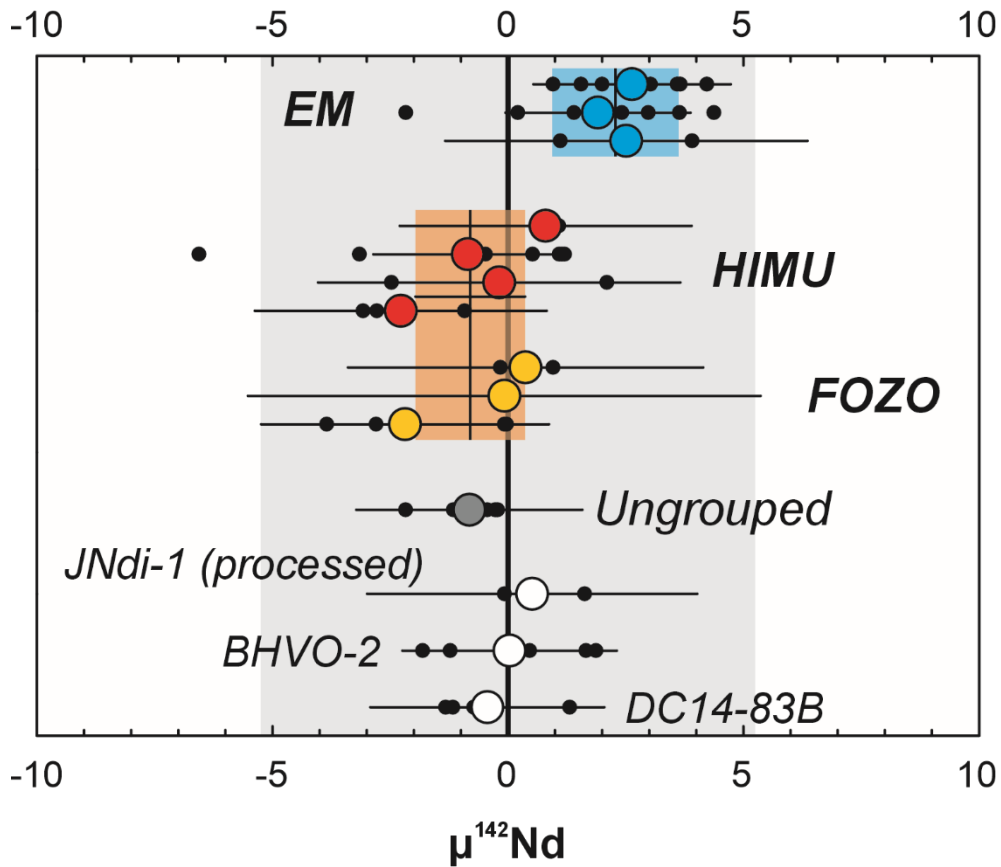
271

272 **Acknowledgements**

273 Funding for this project was provided by ETH Zürich/Marie Skłodowska-Curie Actions
274 COFUND (18-1 FEL-28 to BJP) and the Swiss National Science Foundation (PZ00P2_180005
275 to BJP and project 200021_208079 to MS). The authors thank A. Giuliani and C. Walton for
276 informative discussions and C. Maden for technical assistance with the TIMS.



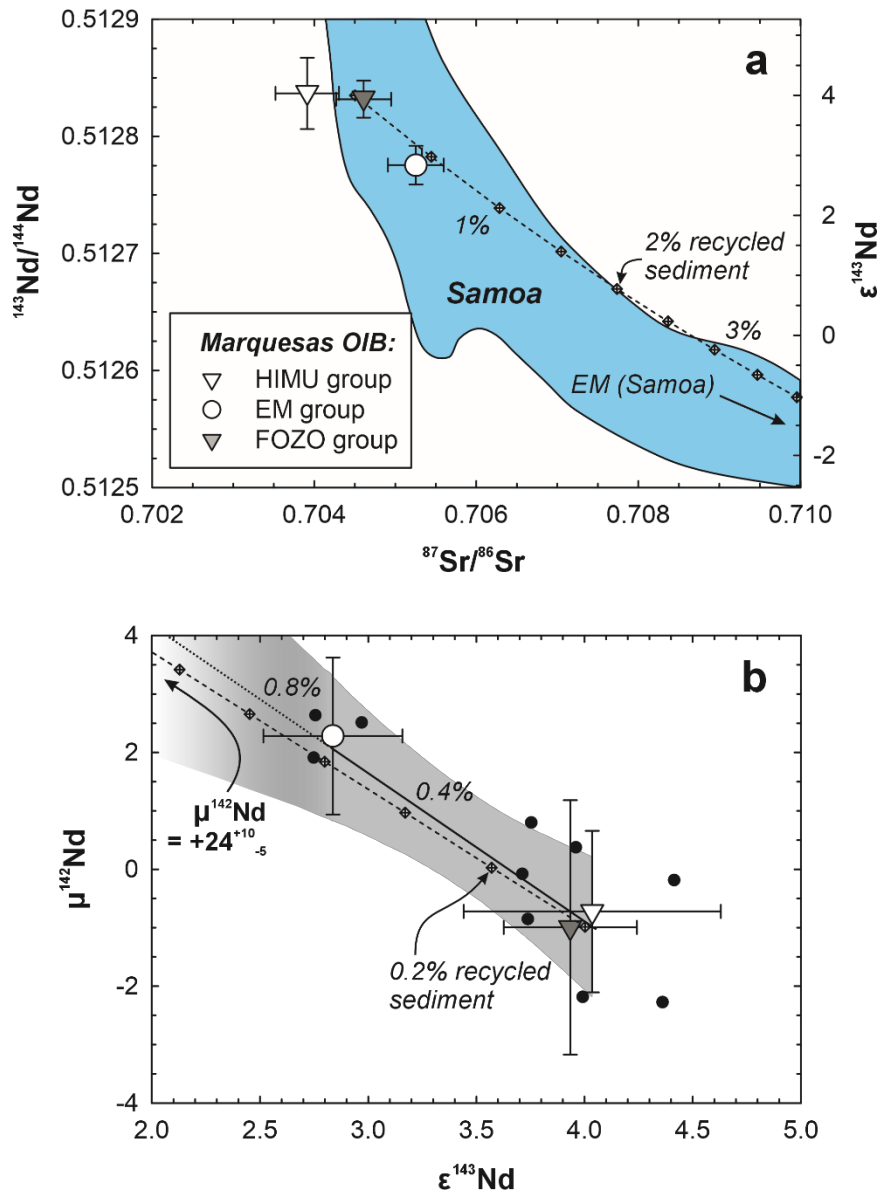
280 **Figure 1.** Isotopic compositions of Marquesas lavas (this study and Castillo et al., 2007; **Table**
 281 **S1**) compared with compositional ranges of global volcanic hotspots (data from GEOROC
 282 precompiled datasets, December 2023 versions). The approximate locations of recognized
 283 mantle components DMM (depleted mid-ocean ridge basalt mantle), HIMU (high- $^{238}\text{U}/^{204}\text{Pb}$ or
 284 high- μ), and EM (enriched mantle) are shown for reference. Neodymium isotopic compositions
 285 in ϵ notation are normalized to the chondritic uniform reservoir [52]; helium isotopic
 286 compositions are normalized to the $^3\text{He}/^4\text{He}$ ratio of air (R_A , 1.38×10^{-6} [53]). For a comparison
 287 of data for Marquesas lavas in this study and in the literature, see **Figure S2**.



289

290 **Figure 2.** Neodymium-142 compositions of Marquesas lavas (normalized to the Nd standard
 291 JNdi-1, in parts per million), the Nd standard processed through separation chemistry, and
 292 reference materials (BHVO-2, DC14-83B). Black points show the results of individual
 293 measurements, colored symbols and error bars show the average and 95% confidence intervals
 294 of samples. Gray shaded region shows the average medium-term (1-2 years) 2σ standard
 295 deviation of Nd standard measurements. Colored shaded regions show the averages and 95%
 296 confidence intervals for sample groups determined by their long-lived radiogenic isotopic
 297 compositions (Supplementary Information).

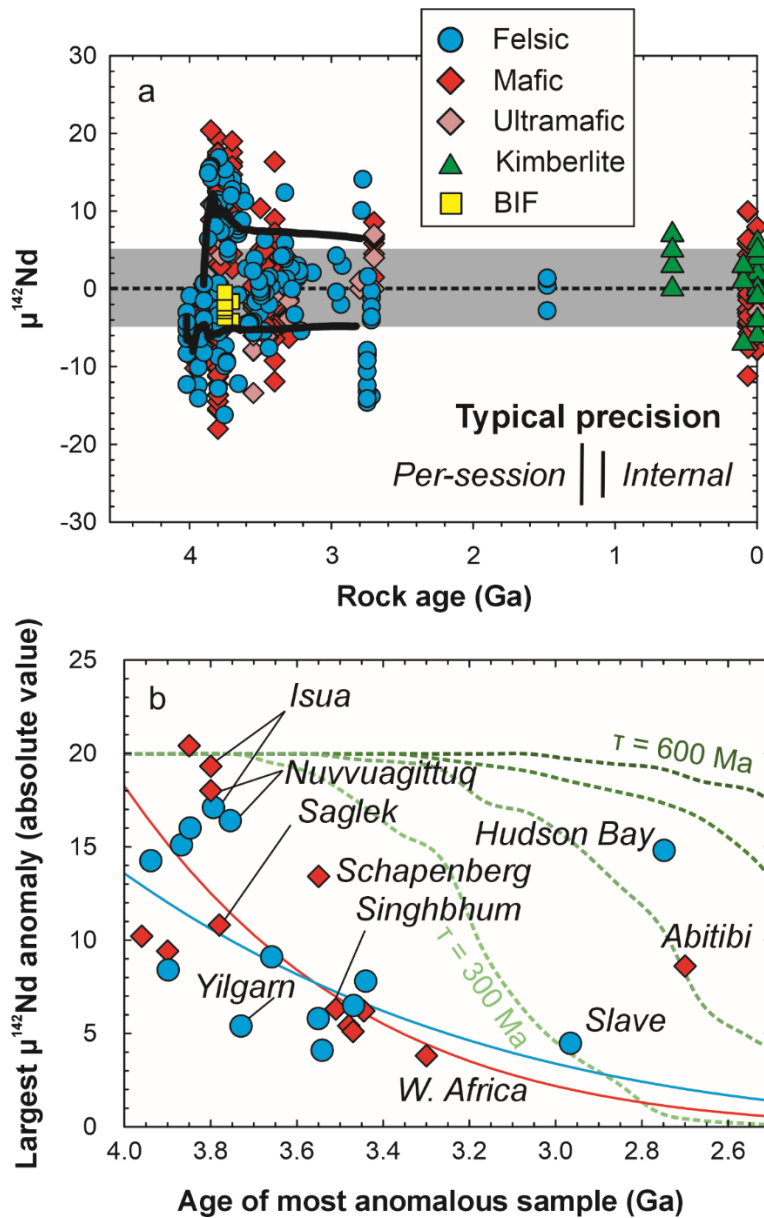
298



299

300 **Figure 3.** Mixing models (dashed lines) for the Sr-Nd isotopic compositions of Marquesas lavas
 301 assuming that the Sr- ^{143}Nd isotopic composition of the EM endmember mirrors that of the
 302 Samoa hotspot ([34], cf., [39]). The solid black line and gray shaded region in (b) represent the
 303 York-type linear regression and 95% confidence interval, respectively, of the $\mu^{142}\text{Nd}$ - $\epsilon^{143}\text{Nd}$
 304 data for Marquesas lavas [33]. The dotted black line and tapered gray shading represent an
 305 extrapolation of this regression. Large symbols and error bars show the per-group average and
 306 95% confidence intervals, black circles show the per-sample measurements. The fraction of
 307 mixed EM component is noted by diamonds along the dashed mixing line. The compositional
 308 range of Samoa EM-type lavas is shown by the blue field (GEOROC database precompiled file,
 309 December 2023 version).

310



311
 312 **Figure 4.** Compilations of published $\mu^{142}\text{Nd}$ data: (a) per-sample data with cumulative average
 313 ages and positive and negative $\mu^{142}\text{Nd}$ populations are shown by bolded black lines. Note that
 314 these include modern samples, but the strong bias of available data toward Eo- and Paleorchean-
 315 aged rocks truncates the cumulative average age at ca. 2.8 Ga. (b) Ages and largest $\mu^{142}\text{Nd}$
 316 anomalies for well-studied Archean crustal localities, with regression curves for felsic and
 317 mafic samples (excluding Hudson Bay and Abitibi). Strongly anomalous $\mu^{142}\text{Nd}$ compositions
 318 (ca. $-5 \leq \mu^{142}\text{Nd} \leq +5$) largely disappeared by the end of the Paleorchean Era. Maximum $\mu^{142}\text{Nd}$
 319 values predicted by the stirring models of [44] are shown for reference as dashed green lines
 320 with τ (stirring rates) of 300, 400, 500, and 600 Ma. Compiled data from [16, 19, 35, 40-43, 45]
 321 and additional references listed in the Supplementary Information.

323

Supplementary information, figures, and tables for:

324

Hadean-aged felsic sediments recycled through the deep mantle by early plate tectonics

325

326

Bradley J. Peters, Marc C. Halfar, Courtney J. Rundhaug, Paterno Castillo, Maria

327

Schönbächler

328

329 **Materials and Methods**

330 *Samples*

331 Samples analyzed for their $^{142,143}\text{Nd}/^{144}\text{Nd}$ ratios were collected from the Marquesas
332 Archipelago (South Pacific Ocean) by Harmon Craig (formerly Scripps Institution of
333 Oceanography) and comprise eight samples from the island of Hiva Oa, two from Fatu Hiva,
334 and one from Nuku Hiva. The Marquesas Islands display geographically age-progressive
335 eruption chronology: the oldest lavas were erupted at the northwestern end of the archipelago
336 (Eiao Island) ca. 5 Ma ago, and the youngest known lavas were erupted at its southeastern side
337 (Fatu Hiva) ca. 1 Ma ago [54]. The archipelago overlies the Pacific large low shear wave
338 velocity zone (LLSVP) and is fueled by a mantle plume that can be imaged by seismic
339 tomography through at least half of Earth's mantle [22]. It is also likely underlain by an ultra-
340 low velocity zone (ULVZ), which contains dense, likely Fe-rich material [55]. For these
341 reasons, the Marquesas hotspot is typically considered to be one of Earth's primary hotspots
342 that taps deep mantle reservoirs observed in its geochemical compositions.

343 Except for sample HO-AT-Gabbro, the samples considered in this study, along with
344 additional samples from Fatu Hiva and Nuku Hiva, were studied by [37] (He-Sr- ^{143}Nd -Pb
345 isotopic compositions) and [28] (^{187}Os isotopic compositions and highly siderophile element
346 abundances). A subset of the samples considered here were studied in [30] (Nd and W isotopic
347 compositions). The sample powders used in this study are aliquots of those used in [37] and the
348 Sr- ^{143}Nd -Pb isotopic compositions of these samples determined in this study are consistent with
349 what was reported in [37] (**Table S1**). The Nd isotopic data presented in this manuscript is
350 expanded from those reported in [30] and includes new Sr- $^{142,143}\text{Nd}$ -Pb isotopic analyses. The
351 samples in this study are alkali basalts ($\text{SiO}_2 = 45.0 - 48.3$ wt.%, $\text{Na}_2\text{O} + \text{K}_2\text{O} = 2.3 - 5.3$ wt.%
352 across all samples). Because the samples were originally intended for study of noble gases, they
353 are exclusively fresh, olivine-phyric and represent surficial flows primarily from the post-shield
354 stage of the islands.

355 The Sr- ^{143}Nd -Pb isotopic compositions of the samples in this study overlap those of
356 literature data for the Marquesas Islands and mirror their trends (**Figure S2**) but do not capture
357 some of the highest $^{87}\text{Sr}/^{86}\text{Sr}$ ratios (up to 0.7065, this study up to 0.7054) and lowest $\epsilon^{143}\text{Nd}$
358 compositions (down to +1.2, this study down to +2.6) recorded in some published data (e.g.,
359 [27, 56-58]). Together, the published and new Sr- ^{143}Nd isotopic compositions define a trend
360 roughly connecting a moderately depleted composition (similar to HIMU or the mantle focal
361 zone, FOZO, also known as C, common component, and PREMA, prevalent mantle; e.g., [59])
362 to an enriched composition, paralleling the trend of Samoa OIB towards an enriched mantle 2

363 (EM2)-like endmember (**Figure 1**; cf., [34]). A subset of samples, primarily from the island
364 Fatu Hiva, trend toward radiogenic Pb isotopic compositions in the direction of HIMU (e.g.,
365 Mangaia; [60]). It is notable that, regardless of their He-Sr-¹⁴³Nd-Pb isotopic compositions, all
366 of these samples display nearly constant and relatively unradiogenic ¹⁸⁷Os/¹⁸⁸Os ratios [28].
367 These authors interpreted this signature as reflecting a dominant role for Os-rich peridotite
368 lithologies in the overall Os budget of Marquesas lavas, and a relatively unimportant role for
369 Os-poor and incompatible-rich source components like EM. Since the Os isotopic compositions
370 of Marquesas lavas do not participate in the mixing trends that are clear in the Nd isotopic data,
371 they are not considered in the sample grouping process or the interpretation of $\mu^{142}\text{Nd}$ data using
372 these mixing trends.

373 There is also significant variability in ³He/⁴He ratios among Marquesas lavas [37].
374 Samples from Fatu Hiva have MORB-like ($8 \pm 2 R_A$; [53]) to low ³He/⁴He ratios (to 6.8 R_A), a
375 characteristic again associated with HIMU-type OIB. By contrast, samples from Hiva Oa show
376 MORB-like to elevated ³He/⁴He ratios (to 14.4 R_A). Elevated ³He/⁴He ratios are commonly
377 associated with moderately depleted Sr-¹⁴³Nd-Pb isotopic compositions that are similar to the
378 global FOZO component. Among Marquesas lavas, the highest ³He/⁴He ratios are associated
379 with moderately depleted $\epsilon^{143}\text{Nd}$ values around +4. However, one sample (HO-AT-3) with
380 elevated ⁸⁷Sr/⁸⁶Sr ratios and lower $\epsilon^{143}\text{Nd}$ compositions that trend toward an EM endmember
381 also possesses a ³He/⁴He ratio greater than the MORB range.

382 These isotopic characteristics permit the division of the samples into groups that are
383 most characteristic of the FOZO, HIMU, and EM mantle components. In the EM group are two
384 samples from the Puamau Bay area of Hiva Oa (HO-PUA-2 and HO-PUA-3) that strongly
385 overlap with the Ua Huka group of [27] (**Figure S2**), along with other young Hiva Oa samples
386 that are characteristic of the Puamau Bay area. The third member of the EM group is sample
387 HO-AT-4, which was collected in the center of Hiva Oa and also strongly overlaps with the Ua
388 Huka group. This group has high ⁸⁷Sr/⁸⁶Sr ratios (>0.7051), low $\epsilon^{143}\text{Nd}$ values (<3.0), and
389 ³He/⁴He ratios overlapping with the upper range of MORB. The HIMU group is composed of
390 two samples from the Hanaiapa Bay area of Hiva Oa (HO-HI-2 and HO-HI-3) and two samples
391 from Fatu Hiva (FH-OM-3 and FH-TOP), all of which strongly overlap the Fatu Hiva group of
392 [27] (**Figure S2**) for their ⁸⁷Sr/⁸⁶Sr, ¹⁴³Nd/¹⁴⁴Nd, and ²⁰⁶Pb/²⁰⁴Pb isotopic compositions. The
393 samples from Hiva Oa have ²⁰⁶Pb/²⁰⁴Pb ratios greater than 19.35, and those from Fatu Hiva
394 have ²⁰⁶Pb/²⁰⁴Pb ratios greater than 19.60. The FOZO group is comprised of two samples from
395 the village of Atuona on Hiva Oa (HO-AT-1 and HO-AT-Gabbro) and the single sample from
396 Nuku Hiva (NH-HA-1). Like other samples from these localities, they strongly overlap with

397 the Ua Huka group of [27] (**Figure S2**) and have lower $^{206}\text{Pb}/^{204}\text{Pb}$ ratios (< 19.2) than Hiva Oa
398 samples with HIMU affinity. Sample HO-AT-1 additionally has a $^3\text{He}/^4\text{He}$ ratio ($14.4 \pm 1.4 R_A$)
399 that is statistically higher than MORB. It is notable that both samples from the FOZO and EM
400 groups strongly overlap with the Ua Huka group trends of [27] whereas the HIMU group
401 overlaps the Fatu Hiva group trends (**Figure S2**). However, together these samples define a
402 single sublinear trend in He-Sr- ^{143}Nd -Pb isotopic diagrams that transverses the Fatu Hiva and
403 Ua Huka trends; thus, we find it more straightforward to interpret the samples in terms of
404 commonly used isotopic components (FOZO, EM, and HIMU) rather than utilizing the Fatu
405 Hiva and Ua Huka trends. This choice does not contradict the existence of these isotopic
406 “stripes” [27]. Instead, it merely parameterizes their componentry using well-studied mantle
407 components rather than the more sophisticated componentry analysis of [27]. In this sense, the
408 effect of the grouping on $\mu^{142}\text{Nd}$, which we later discuss in terms of a stronger (EM group)
409 versus weaker (FOZO + HIMU) EM components could instead be reframed as a stronger versus
410 weaker B or D component in their terminology, where both B and D both trend toward an EM2-
411 or Samoa-like component. The FOZO group would then be described as having a stronger A
412 component along the Ua Huka trends, which [27] interpreted as being intrinsic to the Marquesas
413 plume, and the HIMU group possesses a stronger C component (not to be confused with the C
414 or FOZO component) along the Fatu Hiva trends. Some Ua Huka trends imply that the A
415 component of [27] may be relatively ^{206}Pb -rich. However, such a trend is not visible in our data
416 that otherwise have Sr- ^{143}Nd - ^{206}Pb isotopic compositions that overlap the Ua Huka trends
417 (**Figure S2**).

418 There are four samples from [37] that do not easily fit into the FOZO, EM, or HIMU
419 isotopic groups. Three of these samples are from Fatu Hiva (FH-HV-2, FH-HV-3, FH-OM-1),
420 and have elevated $^{206}\text{Pb}/^{204}\text{Pb}$ (>19.5) ratios, which are characteristic of the HIMU group.
421 However, they have generally lower $^{87}\text{Sr}/^{86}\text{Sr}$ ratios (<0.7038) and substantially higher $\epsilon^{143}\text{Nd}$
422 values ($> +5.6$) than the HIMU group, which places these samples closer to the Ua Huka trends
423 of [27] (**Figure S2**), rather than the Fatu Hiva trends that are associated with most HIMU-type
424 Marquesas lavas. Sample HO-AT-3 was collected from the same locality as sample HO-AT-1
425 (FOZO group), and it likewise has a $^3\text{He}/^4\text{He}$ ratio ($11.8 \pm 1.4 R_A$) that is statistically higher than
426 MORB. However, unlike the FOZO group samples, HO-AT-3 has an elevated $^{87}\text{Sr}/^{86}\text{Sr}$ ratio
427 (0.705306 ± 0.000006) and a lower $\epsilon^{143}\text{Nd}$ composition ($\epsilon^{143}\text{Nd} \approx +3$), which are intermediate
428 to the compositions of the EM and FOZO groups. Of the four ungrouped samples, this was the
429 only one measured for its $\mu^{142}\text{Nd}$ composition, which strongly overlaps with the combined
430 FOZO and HIMU group average (**Table S1**). However, due to the ambiguous long-lived

431 isotopic signature of this sample, its $\mu^{142}\text{Nd}$ composition is excluded from interpretation (see
432 also later discussion of statistical treatment of sample grouping).

433

434 *Sample dissolution and general sample treatment*

435 Samples digested for Sr and Pb isotopic measurements, but not reference materials, were
436 leached in 2M HCl at 60°C for about one hour prior to digestion. Samples digested for Nd
437 isotopic measurements were not leached, following the methods of previous ^{142}Nd studies (e.g.,
438 [16, 61]). All samples were dissolved in a mixture of 4:1 ultrapure HF and double-distilled
439 HNO_3 in 15 mL Savillex Teflon jars on a Teflon-coated hotplate at 140°C. Typically, complete
440 dissolution was achieved in 1-3 days; in some cases, refractory dark grains remained, and in
441 these cases the dissolution step was repeated. Samples were then taken up in solutions of 6-8M
442 HCl and refluxed for 1-2 days on a Teflon-coated hotplate at 120°C. In most cases, this step
443 was sufficient to break up residual solid fluorides and produce transparent sample solutions,
444 however in some cases this step had to be repeated one or more times to obtain transparent
445 solutions. All chemical procedures described below utilized ultrapure (H_2O , HF, H_3PO_4) or
446 double-distilled (HCl, HNO_3) reagents and precleaned Teflon sample containers.

447

448 *Neodymium separation and Nd isotopic measurements*

449 Neodymium was separated from matrix elements and other rare earth elements (REE,
450 especially Ce and Sm) using methods modified from [61-63]. In the first method (cf., [61]),
451 matrix separation was achieved using Bio-Rad AG® 50W-X8, 200-400 mesh cation resin, and
452 Ce separation was achieved by oxidizing the sample with NaBrO_3 and then separating Ce with
453 Eichrom LN resin (50-100 μm). Residual Na from the NaBrO_3 was separated again using Bio-
454 Rad 50W-X8 cation resin (200-400 mesh), then Nd was separated from remaining REE on a 6
455 mm inner diameter x 12 cm length Teflon column filled with Eichrom LN resin (20-50 μm). In
456 the second method (cf., [63]), matrix separation again used Bio-Rad AG® 50W-X8, 200-400
457 mesh cation resin. For Ce and Sm separation, a column containing Eichrom DGA resin
458 (normal/unbranched, 50-100 μm) was positioned directly under a column containing LN resin
459 in a “tandem” configuration. The sample was oxidized with NaBrO_3 and passed onto the upper
460 LN column. The eluate from this column was allowed to drip directly onto the DGA column,
461 where residual Na was then removed using additional 3M HNO_3 . Following this, Nd was
462 separated from other REE using 0.5-2.5M HCl solutions. Yields for the first method were
463 typically 70-90% and yields for the second method were typically 80-95%; in both cases, most
464 Nd was lost during the procedures utilizing cation resin. For this reason, the second method was

465 again modified so that matrix separation was instead accomplished using DGA resin
466 (normal/unbranched, 50-100 μm ; cf., [62]), and a third step utilizing a long-aspect (6 mm ID x
467 6 cm length) Teflon column filled with DGA resin (normal/unbranched, 50-100 μm) was added.
468 In all cases, these methods typically resulted in measured $^{140}\text{Ce}/^{144}\text{Nd}$ and $^{147}\text{Sm}/^{144}\text{Nd}$ ratios
469 that were similar to the JNdi standard. However, the third method utilizing the long-aspect DGA
470 column also produced $^{141}\text{Pr}/^{144}\text{Nd}$ ratios that were typically $<1 \times 10^{-4}$, whereas the first two
471 methods typically produced measured $^{141}\text{Pr}/^{144}\text{Nd}$ ratios that were between 5×10^{-2} and 1 (i.e.,
472 2-4 orders of magnitude higher).

473 For each method, the effects of the separation chemistry on isotopic compositions were
474 monitored by repeated separations and measurements of the BHVO-2 reference material and
475 by processing the JNdi standard through the chemistry procedure (**Figure S5**). In the case of
476 BHVO-2, a separation utilizing the first method yielded $\mu^{142}\text{Nd} = +1.7 \pm 5.4$ (2σ standard
477 deviations, s.d., external, $n = 1$; see below for an explanation of precision reporting), separations
478 utilizing the second method yielded $\mu^{142}\text{Nd} = +0.1 \pm 2.9$ (95% c.i., MSWD = 0.2, $n = 4$), and a
479 separation utilizing the third method yielded $\mu^{142}\text{Nd} = -1.8 \pm 5.2$ (2σ s.d. external, $n = 1$).
480 Together, these analyses yielded an overall average for BHVO-2 of $\mu^{142}\text{Nd} = 0.0 \pm 2.3$ (95% c.i.,
481 MSWD = 0.3, $n = 6$) and $\epsilon^{143}\text{Nd}_{\text{CHUR}} = +6.73 \pm 0.018$ (95% c.i., MSWD = 0.8, $n = 5$), the latter
482 of which agrees with the preferred GeoREM [64] value of $+6.8 \pm 0.5$. In the case of JNdi
483 processed through separation chemistry, the first method yielded $\mu^{142}\text{Nd} = +1.6 \pm 6.6$ (2σ s.d.
484 external, $n = 1$), the second method yielded $\mu^{142}\text{Nd} = +0.3 \pm 6.8$ (2σ s.d. external, $n = 1$), and the
485 third method yielded $\mu^{142}\text{Nd} = -0.1 \pm 5.2$ (2σ s.d. external, $n = 1$) for overall averages of $\mu^{142}\text{Nd}$
486 $= +0.5 \pm 3.5$ (95% c.i., MSWD = 0.1, $n = 3$) and $\epsilon^{143}\text{Nd}_{\text{CHUR}} = -10.27 \pm 0.03$ (95% c.i., MSWD
487 $= 2.7$, $n = 3$). An in-house standard, DC14-83B (a lamprophyre from the Deccan Traps) was
488 additionally processed through the first ($n = 3$) and second ($n = 2$) separation methods and
489 yielded an overall average $\mu^{142}\text{Nd} = -0.4 \pm 2.5$ (95% c.i., MSWD = 0.2, $n = 5$) and $\epsilon^{143}\text{Nd} = -$
490 1.50 ± 0.04 (95% c.i., MSWD = 2.5, $n = 5$) with no significant difference between the separation
491 methods (**Figure S5**). For all three materials, separation methods 2 and 3 yield $\epsilon^{143}\text{Nd}$
492 compositions slightly higher than, but within analytical uncertainty of, the $\epsilon^{143}\text{Nd}$ compositions
493 produced from separation method 1. Such differences in Nd isotopic compositions may be
494 generated by mass-dependent effects arising from the behavior of Nd on separation resins,
495 however for the observed difference of <6 ppm, the corresponding effect on measured
496 $^{150}\text{Nd}/^{144}\text{Nd}$ ratios would be ca. -50 ppm (cf., [61]), which is greater than analytical uncertainty
497 and not observed in the data. Further, the observed offsets are less than analytical uncertainty
498 for the respective measurements (**Figure S5** and **Tables S2** and **S3**). It is thus evaluated that

499 there are no meaningful differences in data generated for samples processed through the
500 different separation methods and no differences attributable to mass-dependent fractionation
501 effects arising during resin-assisted chemical separation. The strong agreement between
502 measured Nd isotopic compositions of samples processed through different chemical separation
503 methods also attests to their robustness (**Tables S2 and S3**).

504 Residual effects from the chemical separation were also tested observationally. There is
505 no correlation between the total procedural yield of BHVO-2 and any measured Nd isotopic
506 composition that is resolvable outside of analytical error (**Figure S6**). One BHVO-2 replicate
507 with a yield of ca. 79% has coincident negative $\mu^{148}\text{Nd}$ and $\mu^{150}\text{Nd}$, neither of which are
508 resolvable from 0 given the medium-term or 2σ s.d. of JNdi-1 standards run in the same session.
509 Coincident negative $\mu^{148}\text{Nd}$ and $\mu^{150}\text{Nd}$ signatures are an expected result of mass-dependent
510 fractionation effects arising from LN-resin, although it is expected only at very low yields [61,
511 65]. However, this effect would also be expected to produce positive offsets in $\epsilon^{143}\text{Nd}$ [61],
512 whereas this sample has a $\epsilon^{143}\text{Nd}$ composition that is indistinguishable from samples that have
513 $\mu^{148}\text{Nd}$ and $\mu^{150}\text{Nd}$ signatures very close to zero (**Table S3**). The effects of mass-dependent
514 effects arising from chemistry on $\mu^{142}\text{Nd}$ are proportionally much smaller in magnitude than the
515 effects on $\mu^{148}\text{Nd}$ and $\mu^{150}\text{Nd}$, and this sample shows no statistically resolvable difference in
516 $\mu^{142}\text{Nd}$ compared to other measurements of BHVO-2 (**Table S3**). It is therefore assessed that
517 coincident $\mu^{148}\text{Nd}$ and $\mu^{150}\text{Nd}$ deficits up to the magnitude observed in this measurement
518 ($\mu^{148}\text{Nd} = -12.3 \pm 10.8$ and $\mu^{150}\text{Nd} = -39 \pm 35$) are unlikely to affect $\mu^{142}\text{Nd}$ or $\epsilon^{143}\text{Nd}$; in any
519 case, deficits of this magnitude are never observed in our sample data.

520 Cerium and Sm doping tests were also performed to test the effectiveness of interference
521 corrections on $^{142}\text{Nd}/^{144}\text{Nd}$ and $^{143}\text{Nd}/^{144}\text{Nd}$ ratios (**Figure S7**). In all cases, JNdi-1 standards
522 doped with Ce or Sm yielded Nd isotopic ratios that were within the medium-term and session
523 2σ standard deviation for all undoped and unprocessed JNdi-1 standards. However, some
524 possible trends may be observed. For all measured $^{140}\text{Ce}/^{144}\text{Nd}$ ratios ($<7 \times 10^{-4}$), the measured
525 $^{142}\text{Nd}/^{144}\text{Nd}$ ratios are within 3 ppm of the average of all undoped standards measured in that
526 session. However, JNdi-1 standards with higher $^{147}\text{Sm}/^{144}\text{Nd}$ also display progressively higher
527 $^{142}\text{Nd}/^{144}\text{Nd}$ and $^{143}\text{Nd}/^{144}\text{Nd}$ ratios. These correlations imply that the Sm interference correction
528 for ^{144}Nd begins to fail at relatively low levels of Sm, perhaps for $^{147}\text{Sm}/^{144}\text{Nd} > 1 \times 10^{-5}$, and
529 that the assumed $^{144}\text{Sm}/^{147}\text{Sm}$ ratio used for this correction (0.205034) results in a slight
530 overcorrection and thus slightly higher $^{142,143}\text{Nd}/^{144}\text{Nd}$ ratios. Notwithstanding, there is no
531 correlation between measured $^{147}\text{Sm}/^{144}\text{Nd}$ and $^{145}\text{Nd}/^{144}\text{Nd}$, $^{148}\text{Nd}/^{144}\text{Nd}$, or $^{150}\text{Nd}/^{144}\text{Nd}$ ratios
532 (the latter two of which are most strongly affected by Sm interferences), and it is again

533 emphasized that in all cases the measured $^{142}\text{Nd}/^{144}\text{Nd}$ and $^{143}\text{Nd}/^{144}\text{Nd}$ ratios of Sm-doped
534 standards were within the 2σ s.d. of the undoped standards in the same session, implying that
535 this observed correlation may be erroneous. Throughout this study, no measured sample
536 possessed a measured $^{147}\text{Sm}/^{144}\text{Nd}$ ratio greater than the minimum threshold value of 1×10^{-5}
537 nor a measured $^{140}\text{Ce}/^{144}\text{Nd}$ ratio greater than the minimum threshold value of 7×10^{-4} evaluated
538 in these doping tests. Thus, neither Ce nor Sm interferences impact our data in a meaningful
539 way.

540 Total procedural blanks (TPB) were monitored periodically throughout the study. These
541 yielded Nd blanks of 12-29 pg ($n = 3$). Wash eluates were also regularly monitored from the
542 DGA resin, since it is known to have a significant Nd memory effect [62], and these contained
543 up to ca. 200 pg Nd. The tests document the effectiveness of our cleaning method, but
544 nevertheless raise the concern that some of this Nd could be released into sample solutions
545 without detection in our TPB analyses. Thus, these tests were used to determine the maximum
546 number of times the DGA resin was reused before being discarded: for the primary matrix
547 separation, Ce separation, and La-Pr separation on the long aspect columns, the resin was used
548 a maximum of 3, 5, and 7 times respectively. Sample HO-AT-Gabbro contained the least
549 processed Nd at ca. 200 ng, such that in the worst case the wash blank would represent up to
550 0.1% of processed Nd. The remainder of the samples have high Nd abundances (>20 ppm),
551 such that a more typical blank (based on the TPB) would represent $<0.002\%$ of the Nd processed
552 through chemistry. Thus, blanks do not affect measured Nd isotopic compositions and no blank
553 corrections are performed on the data.

554 Isotopic measurements were carried out using the Thermo Scientific Triton thermal
555 ionization mass spectrometer (TIMS) in the Isotope Geochemistry and Cosmochemistry group,
556 Institute of Geochemistry and Petrology, ETH Zürich. Before sample loading, 0.3 μL of 0.1M
557 H_3PO_4 was evaporated to near dryness on 99.99-99.999% purity Re filament. Samples were
558 dissolved in 2M HCl and loaded directly onto the residual liquid H_3PO_4 in aliquots of ~ 0.2 μL .
559 Between each aliquot loading, the liquid was partially dried under a current of 0.7-1.0 A, and
560 this typically resulted in final spot sizes of 0.5-1.5 mm. Measurements utilized nine Faraday
561 cups in a 1 amu spacing configuration and equipped with 10^{11} Ω amplifiers (cf., [61]). The
562 measurement was performed in cycles of four lines each, with masses 143, 144, 145, and 146
563 sequentially directed into the center cup. This results in two dynamic $^{142}\text{Nd}/^{144}\text{Nd}$, $^{143}\text{Nd}/^{144}\text{Nd}$,
564 and $^{148}\text{Nd}/^{144}\text{Nd}$ ratios, three dynamic $^{145}\text{Nd}/^{144}\text{Nd}$ ratios, and one static $^{150}\text{Nd}/^{144}\text{Nd}$ ratio per
565 cycle. Measurements were done without amplifier rotation, and amplifier gain analyses were
566 either performed before each sample (once) or before each measurement session (average of 8-

567 10 separate gain calibrations); both strategies revealed <5 ppm, and often <3 ppm, variability
568 in gain factors across single sessions. A typical measurement consisted of 600 cycles and lasted
569 about 10 hours.

570 Measured Nd isotopic ratios were normalized to a $^{146}\text{Nd}/^{144}\text{Nd}$ ratio of 0.7219 using the
571 exponential law (cf., [61]). A time correction was applied to calculate the $^{146}\text{Nd}/^{144}\text{Nd}$ ratio
572 measured at the same time as the Nd isotopic ratios of interest; for example, to calculate the
573 lines 1-3 dynamic $^{142}\text{Nd}/^{144}\text{Nd}$ ratio, the static $^{142}\text{Nd}/^{144}\text{Nd}$ ratio from line 1 is used and a
574 regression of $^{146}\text{Nd}/^{144}\text{Nd}$ ratios from line 3 versus time (moving window of ± 5 cycles) was
575 used to determine the $^{146}\text{Nd}/^{144}\text{Nd}$ ratio that would be measured in the line 3 configuration at
576 the time when the line 1 $^{142}\text{Nd}/^{144}\text{Nd}$ ratio is integrated (see [61] for further discussion). Runs
577 were further monitored for positive linear increases in $^{146}\text{Nd}/^{144}\text{Nd}$ ratios because deviations
578 from positive linear behavior can indicate that distinct domains are simultaneously ionizing on
579 the filament, which can lead to non-exponential fractionation of Nd isotopes [66]. Whenever
580 non-linear, negatively sloped, or relatively rapid fractionation of $^{146}\text{Nd}/^{144}\text{Nd}$ ratios was
581 observed, the corrected data were manually examined in sections. Anomalous run sections with
582 non-linear $^{146}\text{Nd}/^{144}\text{Nd}$ fractionation were compared to a preferred section from the same run
583 that displayed the most prolonged positive, linear $^{146}\text{Nd}/^{144}\text{Nd}$ fractionation for that run. If any
584 of the average dynamic $^{142,143,145,148}\text{Nd}/^{144}\text{Nd}$ ratios for the anomalous section were statistically
585 resolved from (utilizing the 2σ s.e. of each respective run section) the preferred section, or the
586 corrected $^{142}\text{Nd}/^{144}\text{Nd}$ ratios deviated from exponential-law behavior by more than 30 ppm in
587 the anomalous section, the anomalous section was removed from the data reduction. An
588 example of this filtering method applied to replicate runs of the same sample is shown in **Figure**
589 **S8**. Anomalous $^{146}\text{Nd}/^{144}\text{Nd}$ fractionation requiring data filtering of any degree affected
590 approximately one in five runs. After data filtering, the affected runs always returned dynamic
591 $^{142,143}\text{Nd}/^{144}\text{Nd}$ ratios within uncertainty of the same ratios for replicate runs of the same sample
592 that did not display anomalous $^{146}\text{Nd}/^{144}\text{Nd}$ fractionation. If there was no prolonged period of
593 positive, linear $^{146}\text{Nd}/^{144}\text{Nd}$ fractionation in a run, the entire run was rejected. Independent of
594 fractionation behavior, if the averages of either dynamic $^{142}\text{Nd}/^{144}\text{Nd}$ ratio did not converge by
595 the end of the run i.e., they displayed continuously increasing or decreasing behavior, or
596 oscillating behavior throughout the run, the entire run was rejected. If the combined whole-run
597 average of static lines 1-2 $^{142}\text{Nd}/^{144}\text{Nd}$ ratios, which are respectively used to calculate the
598 dynamic lines 1-3 and 2-4 $^{142}\text{Nd}/^{144}\text{Nd}$ ratios, deviated from exponential-law behavior by more
599 than 5 ppm, the entire run was rejected. Less than 5% of all runs were rejected using these
600 criteria.

601 The ability of our analytical setup to produce Nd isotopic data consistent with those
602 previously obtained at Carnegie Institution for Science [67, 68] was evaluated by re-measuring
603 samples with heterogeneous $\mu^{142}\text{Nd}$ values. A subset of these replicate results was already
604 published and demonstrates strong consistency between the analytical setups at ETH and
605 Carnegie [68]. We further re-measured the compositions of Réunion hotspot lava samples
606 RU0709 and RU0711, which displayed the largest-magnitude positive and negative $\mu^{142}\text{Nd}$
607 compositions, respectively, from replicate measurements undertaken at Carnegie [67]. Our new
608 results are statistically consistent with the previous results (**Table S2**). However, they display
609 somewhat less extreme $\mu^{142}\text{Nd}$ compositions than those previously reported [69]. Including the
610 new results and recalculating replicate statistics as described below, the average $\mu^{142}\text{Nd}$
611 composition for RU0709 is $+5.5 \pm 2.5$ (MSWD = 0.7) and for RU0711 is -7.2 ± 2.7 (MSWD =
612 0.5), thus confirming the presence of strongly heterogeneous $\mu^{142}\text{Nd}$ signatures in the Réunion
613 hotspot mantle source.

614

615 *Data statistics and reporting for Nd isotopic compositions*

616 The external precision for each measurement was estimated as the largest of (1) the 2σ
617 s.e. of all cycles in an individual measurement (typically ca. 2 ppm for dynamic $^{142}\text{Nd}/^{144}\text{Nd}$
618 ratios), (2) the 2σ s.d. of all JNdi-1 standards run in the same barrel as the sample (1.3-6.8 ppm),
619 or (3) the medium-term precision (5.2-6.9 ppm). The medium-term precision is estimated as the
620 2σ s.d. of all JNdi-1 standards run by all instrument users in all barrels over the course of this
621 study, with a correction applied for observed data trends related to the gradual degradation of
622 Faraday cup liners (cf., [61]). The medium-term precision calculation was then reset whenever
623 the Faraday cup liners are replaced; during the course of this study, they were replaced in August
624 2020 and May 2023, meaning that a total of three cup liners were utilized during this study.
625 Medium-term precisions are summarized in **Table S4**. This approach to data precision reporting
626 has several advantages. It permits capturing of instrument or measurement instabilities over
627 short (precision measure 1), medium (precision measure 2), and long (precision measure 3)
628 timescales. For example, the true reproducibility of a single poor-quality measurement within
629 a barrel with generally good-quality measurements will be more accurately captured by the 2σ
630 s.e. of all cycles in an individual measurement (precision measure 1). In comparison, the
631 reproducibility of a good-quality sample measurement within a barrel with many poor-quality
632 measurements will be captured by the 2σ s.d. of multiple standard measurements (precision
633 measure 2), which may capture weeks-scale instrument instabilities not reflected by the 2σ
634 standard error of sample measurements (i.e. 2σ s.e.m.; individual measurements are ca. 12

635 hours long). Long-term instrumental instabilities, including amplifier drift or instability,
636 degradation of internal electrical parts, or inaccurate gain or baseline calibrations can be
637 effectively captured by medium-term reproducibility of JNdi standards (precision measure 3).

638 In practice, the medium-term reproducibility of JNdi standards (precision measure 3) is
639 almost always the largest and therefore the most conservative value. However, its application
640 is statistically justified in hindsight: the typical approach of estimating single-measurement
641 precision using the 2σ s.e.m. alone shows that repeated measurements and repeated digestions
642 are sometimes statistically distinct (i.e. their values do not overlap within 2σ s.e.m. precision),
643 implying that this estimate of measurement uncertainty underestimates the true measurement
644 uncertainty. This can be illustrated, for example, using the Isoplot probability of fit and Model-
645 2 functions (in IsoplotR, this is known as the “random effects model”). Probability of fit
646 calculates the chance that the data uncertainty represent a “true” data array with the same
647 amount of dispersion (according to the composition assigned to each sample) or less. A low
648 probability of fit thus implies that a sample group represents a true data distribution that is more
649 dispersed than the assigned compositions alone, while a high probability of fit implies that the
650 sample group is less dispersed than the assigned compositions. In the case of two measurements
651 that are distinct or nearly distinct considering their respective 2σ s.e.m., but not distinct
652 considering the 2σ s.d. of all standards measured in the same respective barrels, Isoplot will
653 return low probabilities of fit if the input errors reflect the 2σ s.e.m. and higher probabilities of
654 fit for input errors that reflect the 2σ s.d. of all standards from the same barrel. In the former
655 case, the strict statistical interpretation of this result is that the measurements represent two
656 separate sample populations, something that is not expected within single samples for an
657 element like Nd, which is not known to suffer from nuggeting effects. On the other hand,
658 applying uncertainty estimates as described here often results in per-sample MSWD less than 1
659 (**Table S3**), which indicates a possible overestimation of sample uncertainty. We assess that, in
660 the absence of knowing the true uncertainty of any given sample estimate, overestimation of
661 sample uncertainty (thus producing MSWD <1 and larger 95% confidence intervals for
662 replicate sample measurements) is geologically preferable to underestimation of sample
663 uncertainty, which may lead to the inference of heterogeneous isotopic compositions where in
664 reality none exist.

665 For multiple measurements of the same sample that are statistically distinct from each
666 other when considering their respective 2σ s.e.m., Isoplot suggests a Model-2 fit, where it
667 predicts the existence of an unknown, external source of error and estimates its magnitude. In
668 many cases, Isoplot calculates the magnitude of this error source to be similar to the estimated

669 medium-term precision, which is larger than measurement 2σ s.e.m.. This provides
670 circumstantial evidence that this is a closer estimate of the true per-measurement precision than
671 2σ s.e.m. alone. A comparison of replicate sample statistics using the uncertainty determination
672 described here versus the more typical practice of using 2σ s.e.m. alone is provided in **Table**
673 **S5**.

674 It is important to acknowledge that expected $\mu^{142}\text{Nd}$ heterogeneity in modern, mantle-
675 derived rocks is barely larger than analytical precision, although multiple independent studies
676 have verified its existence [16, 44, 67]. Statistically resolving small-scale geochemical
677 heterogeneity is challenging, particularly if the magnitude of medium-term precision is greater
678 than the magnitude of expected sample heterogeneity. This study therefore uses sample
679 replication as a strategy to precisely determine the $\mu^{142}\text{Nd}$ compositions of samples. Sample
680 replication is very time intensive with TIMS analyses, because a single sample digestion may
681 only provide enough Nd for 1-2 measurements, and each measurement duration is ca. 12 hours.
682 Notwithstanding, sample replication is crucial to assess the effect of potentially overestimated
683 or erroneous precision during hypothesis testing. In this context, repeated measurements of
684 samples, which each provide an independent estimate of the effect of random analytical noise
685 and the effects of sample handling that cannot be unambiguously quantified (e.g., filament
686 loading technique), limits the impact of measurement error on overall sample results. However,
687 sample replication cannot infinitely reduce inferred uncertainty on a per-sample basis. For
688 example, assuming that medium-term precision drives the assigned per-sample uncertainty (see
689 discussion above), a numerical simulation yields a typical 95% confidence interval after two
690 sample measurements between ca. 3.5-4 ppm, if the medium-term precision is ca. 5.4 ppm
691 (equal to that for the Faraday cup liners used over most of this study). After five measurements,
692 the 95% confidence interval decreases to ca. 2-3 ppm and approaches a theoretical limit equal
693 to the 2-standard error (s.e.) of replicate measurements. Improved per-sample precision also
694 improves the minimum theoretical 95% confidence interval of sample replicates; for example,
695 a per-sample precision of 3 ppm produces 95% confidence intervals of ca. 1.2-2.2 ppm for $n \geq 5$
696 and a per-sample precision of 2 ppm produces 95% confidence intervals of ca. 0.9-1.7 ppm for
697 $n \geq 5$. Note, however, that a per-sample precision of 2 ppm requires that the medium-term
698 precision, per-barrel 2σ standard deviation of standards, and per-sample internal precision all
699 remain at or below 2 ppm over the temporal course of sample replication.

700 Layered on top of analytical error is additional randomness introduced by geological
701 processes that cannot be realistically quantified on a per-sample basis. For example, samples
702 deriving from the same batch of magma ought to theoretically possess identical $\mu^{142}\text{Nd}$

703 compositions that reflect the $\mu^{142}\text{Nd}$ compositions of their mixed mantle sources, but in practice
704 data that has been analytically well-constrained will still produce different $\mu^{142}\text{Nd}$ compositions
705 for samples that should otherwise be genetically identical. This difference may be produced by
706 small-scale geological processes, such as localized effects from high-temperature mass-
707 independent isotopic fractionation [70], but are nearly untraceable. Higher-order geochemical
708 heterogeneity that exists independent of this geological randomness can be statistically tested
709 by grouping well-constrained samples using independent geochemical or geological data. Such
710 an approach mirrors hierarchical “nested studies,” which are commonly applied in biological
711 and medical studies. For example, samples can be divided according to their isotopic grouping
712 (FOZO, EM, and HIMU), according to island, or can be summarized on a per-hotspot basis.
713 The success of each level of grouping can be assessed for example using Isoplot’s probability
714 of fit model. Evaluating all Marquesas samples together, the probability of fit for $\mu^{142}\text{Nd}$ is 0.08.
715 Samples from the island Hiva Oa, which represent all isotopic groups, have a probability of fit
716 of 0.2 for $\mu^{142}\text{Nd}$. The highest probabilities of fit are returned when the samples are grouped
717 according to their isotopic groups, which were determined by their He-Sr- ^{143}Nd -Pb isotopic
718 compositions (see discussion above). For the EM, HIMU, and FOZO groups, the probabilities
719 of fit for $\mu^{142}\text{Nd}$ are 0.87, 0.56, and 0.54, respectively. The probability of fit for the combined
720 EM and FOZO groups, which display more isotopic likeness than either of these groups
721 compared to the EM group, is 0.76 for $\mu^{142}\text{Nd}$. At all levels of grouping, the probabilities of fit
722 for long-lived radiogenic isotopic systems (He-Sr- ^{143}Nd -Pb) are very low, often <0.01 . This is
723 interpreted as an example of geological randomness as discussed above because these
724 compositions are clearly analytically resolved and long-lived radiogenic isotopes display much
725 more geological heterogeneity (parts per 10^4 or less) than short-lived radiogenic isotopes (parts
726 per 10^5 or more). Changes in $\epsilon^{143}\text{Nd}$ could be locally induced in a single magma batch by, for
727 example, chemical assimilation of materials with distinct $\epsilon^{143}\text{Nd}$ values during fractional
728 crystallization, but such effects are virtually impossible to geologically constrain.

729 To verify that our techniques are able to resolve small-scale $\mu^{142}\text{Nd}$ heterogeneity like
730 that observed between the EM and HIMU/FOZO groups of Marquesas OIB, an analytical
731 “challenge” was designed (**Figure S9**). Using samples with previously well-constrained $\mu^{142}\text{Nd}$
732 compositions from each group, samples that displayed $\mu^{142}\text{Nd}$ signatures of opposite signs
733 (positive vs. negative) were measured in sequence. In this challenge, samples HO-PUA-2 and
734 HO-PUA-2 (EM), NH-HA-1 (FOZO), and HO-HI-3 (HIMU) were utilized. Given the internal
735 precision of each run (1.8-2.8 ppm) and the 2σ standard deviation of all standards run in the
736 same session (1.3 ppm, $n = 5$), both EM samples are statistically resolved from the FOZO

737 sample run before or after. The $\mu^{142}\text{Nd}$ composition of HIMU sample HO-HI-3 is likewise lower
738 than that of each EM sample, but in this case the measurements were not statistically resolved.
739 However, the $\mu^{142}\text{Nd}$ composition of HO-HI-3 determined during the challenge strongly
740 overlaps with the 95% confidence interval of the combined HIMU and FOZO group. The
741 $\mu^{142}\text{Nd}$ value of HO-HI-3 from this run represents one of the highest measured for this sample
742 throughout the study. This result thus illustrates the importance of sample replication to achieve
743 accurate results. These results neglect medium-term precision as the challenge was completed
744 within a short timescale (6 days) and medium-term precision enables comparison of data
745 collected over longer timescales (e.g., the lifespan of the Faraday cups). The overall result of
746 the challenge within the context of medium-term precision can be projected using Isoplot's
747 Model-2 function, which calculates a factor by which to expand the data precision to account
748 for unknown, external controls on the true data precision. Using these calculations, the
749 challenge produced a weighted average for EM sample runs of $\mu^{142}\text{Nd} = +3.4 \pm 1.1$ (MSWD =
750 1.1) and for HIMU and FOZO samples of $\mu^{142}\text{Nd} = -1.5 \pm 2.4$ (MSWD = 5.1; the high MSWD
751 is caused by the somewhat high $\mu^{142}\text{Nd}$ of sample HO-HI-3 measured during the challenge),
752 thus confirming that the two groups are statistically distinct, even if samples from each group
753 are run in sequence within short time proximity.

754

755 *Chemical separation and isotopic measurements of Sr and Pb*

756 Strontium and lead isotopic measurements were performed on the same sample
757 powders, but represent different powder aliquots than those used for ^{142}Nd isotopic
758 measurements due to differences in separation techniques. First, Pb was separated from sample
759 matrix using BioRad® AG 1-X8, 100-200 mesh anion exchange resin using mixed solutions of
760 HNO_3 and HBr . The residual Br^- in the sample matrix aliquot from this separation was then
761 burned off using drops of concentrated HNO_3 , and the sample was then re-equilibrated in HCl .
762 Strontium and other minor elements (including Rb) were then separated from major elements
763 using BioRad® AG 50W-X8, 200-400 mesh cation exchange resin using solutions of 2-2.5M
764 HCl . The Sr-bearing aliquot from this separation was then re-equilibrated in HNO_3 and
765 subjected to a final separation using Eichrom Sr resin and solutions of 0.05-4M HNO_3 . Total
766 procedural blanks for this method were ca. 370 pg for Sr and ca. 20 pg for Pb, which represent
767 <0.1% of sample Sr and Pb.

768 Isotopic compositions of Sr were measured on the Thermo Fisher Scientific Triton
769 TIMS at the Isotope Geochemistry and Cosmochemistry group at ETH Zürich. Ratios of
770 $^{87}\text{Sr}/^{86}\text{Sr}$ were normalized to $^{88}\text{Sr}/^{86}\text{Sr} = 8.375209$ using the exponential law. The corrected

771 sample $^{87}\text{Sr}/^{86}\text{Sr}$ ratios were then normalized to a $^{87}\text{Sr}/^{86}\text{Sr}$ ratio of 0.710245 (mean of published
772 values from the GeoREM database) for the NBS987 standard on a per-session basis. The
773 external precision of the measured $^{87}\text{Sr}/^{86}\text{Sr}$ ratios is estimated to be equivalent to the 2σ s.d. of
774 all NBS987 standards run in the same session as the samples and is equal to 0.000010. The
775 reference material BHVO-2 was measured twice in the same session as the samples and yielded
776 a mean $^{87}\text{Sr}/^{86}\text{Sr}$ ratio of 0.703467 ± 0.000007 , which agrees with the preferred value of
777 GeoREM (0.703478 ± 0.000068). Strontium isotopic compositions for all standards, reference
778 materials, and samples are summarized in **Table S5**.

779 Lead isotopic compositions were measured on the ThermoFisher Neptune inductively
780 coupled plasma mass spectrometer (ICP-MS) of the Isotope Geochemistry and
781 Cosmochemistry group at ETH Zürich. Instrumental mass fractionation was corrected using Tl
782 doping and a $^{203}\text{Tl}/^{205}\text{Tl}$ ratio that is iteratively constrained in order to reduce the sum of offsets
783 between the measured $^{206,207,208}\text{Pb}/^{204}\text{Pb}$ and $^{207,208}\text{Pb}/^{206}\text{Pb}$ compared to the standard NBS881
784 [71] to zero. The external precisions of measured $^{206}\text{Pb}/^{204}\text{Pb}$, $^{207}\text{Pb}/^{204}\text{Pb}$, and $^{208}\text{Pb}/^{204}\text{Pb}$ ratios,
785 defined as the 2σ s.d. of all NBS881 standards run in a given session, were 0.0007-0.0019,
786 0.0007-0.0022, and 0.0020-0.0059, respectively, across three measurement sessions. Repeated
787 measurements of the reference material BCR-2 yielded measured $^{206}\text{Pb}/^{204}\text{Pb}$, $^{207}\text{Pb}/^{204}\text{Pb}$, and
788 $^{208}\text{Pb}/^{204}\text{Pb}$ ratios of 18.7665 ± 0.0001 (GeoREM preferred: 18.754 ± 0.018), 15.6323 ± 0.0001
789 (GeoREM preferred: 15.622 ± 0.010), and 38.7638 ± 0.0004 (GeoREM preferred: 38.726
790 ± 0.044), respectively, in 50 measurements across all three sessions. Repeated measurements of
791 the reference material BHVO-2 yielded measured $^{206}\text{Pb}/^{204}\text{Pb}$, $^{207}\text{Pb}/^{204}\text{Pb}$, and $^{208}\text{Pb}/^{204}\text{Pb}$
792 ratios of 18.6195 ± 0.0002 (GeoREM preferred: 18.634 ± 0.068), 15.5417 ± 0.0001 (GeoREM
793 preferred: 15.524 ± 0.050), and 38.2378 ± 0.0004 (GeoREM preferred: 38.146 ± 0.646),
794 respectively, in 15 measurements across all three sessions. Lead isotopic compositions for all
795 standards, reference materials, and samples are summarized in **Table S6**.

796

797 **Enriched mantle (EM) mixing models**

798 The EM dilution/mixing models presented in **Figure 3** are built on a simple mixing
799 calculation between an assumed Marquesas FOZO-like component ($^{87}\text{Sr}/^{86}\text{Sr} = 0.7045$ and
800 $\epsilon^{143}\text{Nd} = +4.0$, cf., **Figures 1** and **S1**) and an extreme EM representative from the Samoa hotspot
801 (sample ALIA115-21 from [34], cf. [39]). The EM component is selected as the recycled
802 component for this mixing model because it has an elevated $\mu^{142}\text{Nd}$ composition compared to
803 the presumed bulk Earth composition ($\mu^{142}\text{Nd} \equiv 0$), meaning that the bulk Earth composition
804 can be used as an endmember in the envisaged dilution process. By contrast, the Marquesas

805 HIMU group has a $\mu^{142}\text{Nd}$ signature that strongly overlaps the bulk Earth value. This means
806 that any mixing/dilution model involving HIMU would have to invoke two components with
807 non-zero $\mu^{142}\text{Nd}$ signatures, but no independent basis exists for identifying what components
808 these would be.

809 The mixing models for the Marquesas EM group invoke a Samoa-like EM composition
810 as the presumed non-zero $\mu^{142}\text{Nd}$ endmember based on observed Sr-Nd-Pb isotopic correlations
811 (**Figures S1-S2**). It is noted that the Fatu Hiva trends envisaged by [27] may not point directly
812 toward a Samoa-like endmember (e.g., **Figure S2**). However, all EM-like samples in the
813 Marquesas archipelago lie on the Ua Huka group trends. The Sr and Nd abundances of the
814 FOZO endmember in this calculation were set to the primitive mantle values of [72]. The Sr
815 and Nd concentrations of the EM endmember were set to the median abundances of felsic rock
816 samples from the Baltic Shield, Dharwar Craton, Kaapvaal Craton, North Atlantic Craton,
817 North China Craton, São Francisco Craton, Siberian Craton, Superior Province, and West
818 Australian Craton, where both Rb and Sr or Sm and Nd abundance data were available. These
819 medians were calculated using data available in the December 2023 versions of the precompiled
820 data files of GEOROC, and no temporal trends for element abundance medians are observed
821 across the Archean Eon (**Figure S10**). It is assumed that the Sr and Nd abundances of the
822 subducting material are unchanged compared to the respective elemental abundances of the
823 rocks they derived from; this is consistent with the lack of difference between the Sr and Nd
824 abundances of modern upper continental crust [73] and subduction zone sediments [74]. The
825 Pb isotopic compositions of EM lavas were not modeled because of the susceptibility of Pb and
826 its isotopic compositions to modification by post-eruptive processes.

827 Once the Sr- ^{143}Nd mixing curve was calculated, the closest point along this mixing line
828 to the average of the Marquesas EM group samples was calculated to be ca. 0.6% of the EM
829 endmember (i.e. ca. 99.4% dilution of this component by FOZO). The mixing line was then
830 projected to $\mu^{142}\text{Nd}$ - $\epsilon^{143}\text{Nd}$ space using an assumed $\mu^{142}\text{Nd}$ of FOZO ($\mu^{142}\text{Nd} = -1$, the average
831 of the Marquesas FOZO group) and the highest $\mu^{142}\text{Nd}$ composition recorded by the Marquesas
832 EM group samples (sample HO-PUA-2, $\mu^{142}\text{Nd} = +2.6$), which was fixed to the same mixing
833 proportion as for the Sr- ^{143}Nd mixing model. The $\mu^{142}\text{Nd}$ mixing line was then projected to a
834 100% EM endmember, giving a resulting $\mu^{142}\text{Nd}$ value of +24. The uncertainty on this result
835 (+10/-5) reflects the propagation of the 95% confidence intervals for the $^{87}\text{Sr}/^{86}\text{Sr}$ and $\epsilon^{143}\text{Nd}$
836 compositions of the Marquesas EM group. Model parameters are summarized in **Table S7**.

837 It is important to make two observations about this mixing model. First, it presumes that
838 the EM endmember is comprised only of felsic material (after [39]), whereas the rocks with the

839 highest published $\mu^{142}\text{Nd}$ values ($\geq +16.9$, $n = 8$, [40-42, 75]) are exclusively mafic. Second,
840 the formation of Archean felsic crust presumes the existence of a mafic precursor [4], and thus
841 that Earth's earliest crust must have been mafic before it became felsic. The zircon record
842 implies that felsic material was present at Earth's surface by 4.4 Ga [6], but it is reasonable to
843 assume that a large fraction of mafic material remained at Earth's surface at the end of the
844 Hadean Eon (4 Ga ago). We therefore calculate a refined model to predict compositions of mafic
845 and felsic members of materials subducted into the Marquesas deep mantle source (**Figures S3-**
846 **S4**). For simplicity, it is assumed that the felsic member is a direct product of melting of the
847 mafic endmember, since the two materials would be expected to be spatially proximate [35]. In
848 order to calculate the reciprocal Nd isotopic compositions of these endmembers, a
849 differentiation chronology must be defined (**Figure S4**). It is assumed that initial mantle
850 differentiation to produce an early depleted mantle reservoir occurred 4.37 Ga ago, a globally
851 isochronous date in the Sm-Nd system among Archean-aged rocks [76]. It is further assumed
852 that the final felsic member was formed at 4.1 Ga and that it evolved a $\mu^{142}\text{Nd}$ composition of
853 +16, equal to the highest value measured for a felsic rock [40], and a modern $\epsilon^{143}\text{Nd}$
854 composition of -32, which overlaps the value for Archean crustal composites [77]. The mafic
855 sedimentary member is presumed to have a chondritic modern $\epsilon^{143}\text{Nd}$ composition and Sr and
856 Nd abundances equal to the median of compiled cratonic rocks (using the same GEOROC
857 precompiled files are previously mentioned; **Figure S11**). Like felsic rocks, there are no
858 temporal trends in the Sr and Nd abundances of Archean-Proterozoic mafic rocks (**Figure S11**),
859 so the use of these abundances is considered broadly representative. The timing at which the
860 mafic sedimentary member was extracted from the early depleted mantle reservoir was used as
861 a fitting parameter, as described below. Given these constraints, the mafic sedimentary member
862 must have had a $\mu^{142}\text{Nd}$ value of $+27^{+12}_{-7}$ and subducted material must be ca. 93% mafic. The
863 proportion of mafic sediment would be less if the felsic sediment member had a higher positive
864 $\mu^{142}\text{Nd}$ value or a lower Nd abundance. Dilution of this endmember with primitive component
865 represented by the Marquesas FOZO sample group produces a mixing array that intersects the
866 Marquesas EM group Sm-Nd compositions (**Figure S3**). Because the Sr and Nd abundances of
867 the mafic and felsic sedimentary members affect the elemental composition of the bulk modeled
868 sediment, the total mixing proportion of sediment increases to 1-2% (cf., [28, 30])

869 The chronology and resulting Nd isotopic compositions of the refined model are
870 calculated using a series of error minimization exercises. First, the required fraction of the mafic
871 member required to match the $\epsilon^{143}\text{Nd}$ composition of the EM endmember composition from the
872 first model is calculated given the inputs mentioned above. This fraction is then used to

873 recalculate the Sr-¹⁴³Nd mixing relationship as in the first mixing model and determine the
874 required $\mu^{142}\text{Nd}$ composition of the mafic sedimentary member. Second, the Sm/Nd ratio of the
875 early depleted mantle reservoir is calculated using the assumed time of mantle differentiation
876 (4.37 Ga ago) and to fit the calculated $\mu^{142}\text{Nd}$ composition of the mafic sedimentary member
877 that is eventually extracted from this early depleted mantle reservoir. Then, the Sm/Nd ratio of
878 the extracted mafic magma is calculated to satisfy the assumption that it evolves to a modern
879 chondritic $\epsilon^{143}\text{Nd}$ composition. These calculations are then iterated to produce a mafic magma
880 matching both the required $\mu^{142}\text{Nd}$ and $\epsilon^{143}\text{Nd}$ compositions. Third, the Sm/Nd ratio of the felsic
881 sedimentary member is calculated assuming that it evolves to a modern $\epsilon^{143}\text{Nd}$ composition of
882 -32. Then, the time at which the mafic material is re-melted to form felsic rock is adjusted to
883 match the highest $\mu^{142}\text{Nd}$ in the current rock record (ca. +16, [40]). These two calculations are
884 then iterated to produce a felsic rock matching both the required $\mu^{142}\text{Nd}$ and $\epsilon^{143}\text{Nd}$
885 compositions. The uncertainty on the $\mu^{142}\text{Nd}$ compositions produced by this model were
886 calculated analogously to the first mixing model. All model inputs and intermediate outputs are
887 summarized in **Table S7**.

888 The $\mu^{142}\text{Nd}$ compositions required for the sedimentary components of both the first and
889 refined models are similar to or somewhat higher than the highest measured $\mu^{142}\text{Nd}$ values for
890 any global Archean-aged rock (**Figure S5**). In all global Archean cratons, the highest $\mu^{142}\text{Nd}$
891 signatures are observed early, mostly in the Eoarchean Eon (**Figure S5a**). By extension, the
892 $\mu^{142}\text{Nd}$ values required by the models were only present on Earth in the Eoarchean and before,
893 with the highest probability of materials possessing $\mu^{142}\text{Nd} \geq +20$ before the Archean-Hadean
894 boundary (4 Ga ago). Very few rocks older than 4 Ga old have been measured for $\mu^{142}\text{Nd}$, likely
895 because they have all been remelted or destroyed by erosion or tectonic processes. As time
896 progresses, it is increasingly unlikely that any segment of Archean crust that is eroded in a
897 spatially stochastic manner will result in a sediment with a high, positive $\mu^{142}\text{Nd}$ signature. This
898 is illustrated by the cumulative average $\mu^{142}\text{Nd}$ compositions of published data, which show
899 that even the average Eoarchean rock had a $\mu^{142}\text{Nd}$ composition of only ca. +10. It is thus very
900 unlikely that subduction of sedimentary material with the bulk $\mu^{142}\text{Nd}$ composition required by
901 the models (+24 in the first model and +27 for mafic material in the refined model) would have
902 occurred in the Eoarchean or later.

903 Both models assume that the Marquesas EM endmember is represented by an extreme
904 Samoa-like Sr-¹⁴³Nd-Pb isotopic composition. This would seem to imply that the results of the
905 models predict that Samoa EM-type lavas should have strongly elevated $\mu^{142}\text{Nd}$ signatures.
906 However, this assumption is invalid for several reasons. First, although the EM arrays of many

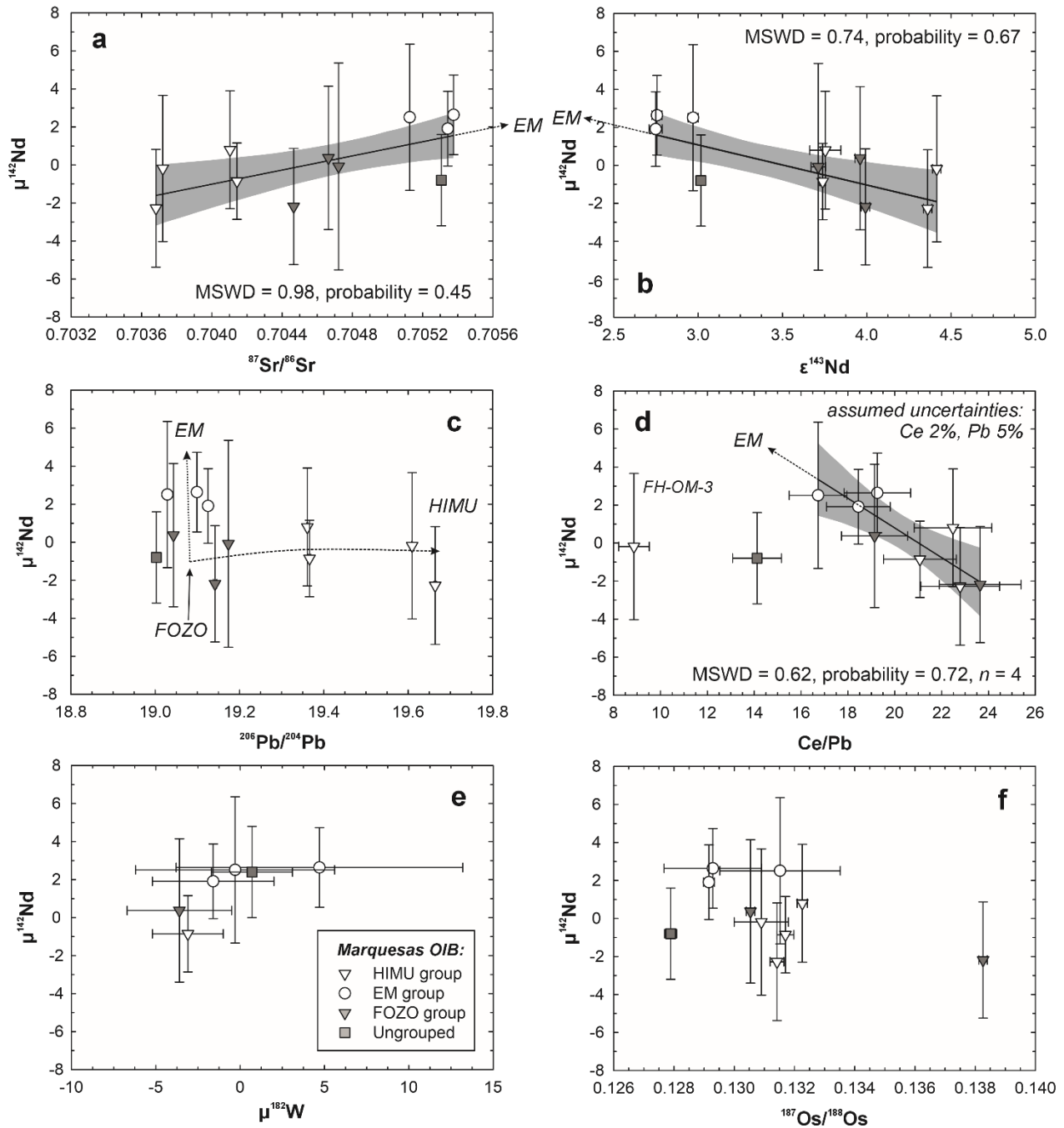
907 global hotspots overlap (e.g., the Pitcairn trend and Ko‘olau group of Hawai‘i), their heritages
908 are often considered to be independent of one another [29, 78], for example representing
909 sedimentary packages of unique blends (e.g., pelagic versus continental) and ages. Second, the
910 mildly elevated $^3\text{He}/^4\text{He}$ signature of Marquesas EM group lavas [37] contrasts with the sub-
911 MORB $^3\text{He}/^4\text{He}$ ratios of Samoa [34]. The two distinct signatures can be reconciled if the EM
912 components of each hotspot have contrasting He abundances (as illustrated in **Figure S2**),
913 however this would imply that they have distinct heritages. Finally, Archean-aged felsic crust
914 is characterized by variable, but uniformly high $^{87}\text{Sr}/^{86}\text{Sr}$ ratios, low $^{143}\text{Nd}/^{144}\text{Nd}$ ratios (e.g.,
915 [77]), and radiogenic Pb isotopic compositions (e.g., [79], for bulk crust). Despite this, Archean-
916 aged crust has highly heterogeneous $\mu^{142}\text{Nd}$ compositions (e.g., [35, 40]). This occurs because
917 long-lived radiogenic isotope systems, such as ^{87}Rb - ^{87}Sr and ^{147}Sm - ^{143}Nd , are decoupled from
918 short-lived systems, such as ^{146}Sm - ^{142}Nd , during any melting or differentiation event that
919 occurred after the lifetime of ^{146}Sm (ca. 500 Ma, i.e. after ca. 4 Ga ago). Events such as melting
920 and metamorphism are fundamental parts of crustal building and will strongly affect Sr- ^{143}Nd
921 isotopic compositions while it is often assumed that they leave $\mu^{142}\text{Nd}$ compositions unchanged.
922 Such isotopic decoupling is therefore a natural consequence of crustal building throughout the
923 Archean. For these reasons, it is possible that the Marquesas and Samoa EM endmembers have
924 Sr- ^{143}Nd -Pb isotopic compositions that are broadly similar, but with distinct $\mu^{142}\text{Nd}$
925 compositions. One submarine lava sample from Samoa with an EM-like isotopic signature has
926 been measured to date, and it did not display an anomalous $\mu^{142}\text{Nd}$ composition [16]. The
927 Marquesas EM component may therefore be unique in this respect and may only be sampled
928 because of the low melt production of the Marquesas hotspot, or other EM hotspots may possess
929 heterogeneous $\mu^{142}\text{Nd}$ signatures, but these have not yet been discovered because high-precision
930 techniques have not yet been applied to these hotspots.

931

932 **References for ^{142}Nd compilation in Figure 4**

933 The global compilation of $\mu^{142}\text{Nd}$ in Figure 4 is not intended to be exhaustive, but it
934 represents all studied environments and comprises the vast majority of all published data. Data
935 sources: [16, 19, 35, 40-43, 45, 75, 76, 80-100].

936

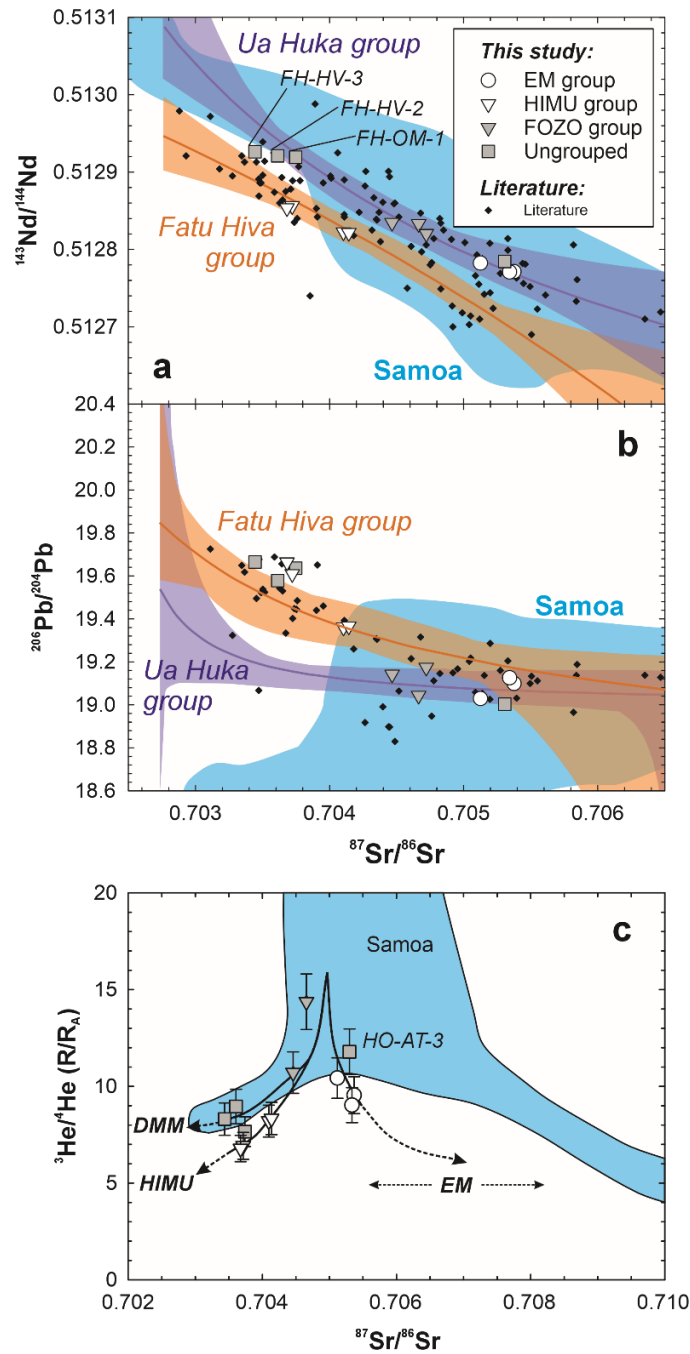


938

939 **Figure S1.** Relationships between the $\mu^{142}\text{Nd}$ and other geochemical and isotopic proxies for the
 940 involvement of distinct mantle components in the source of Marquesas lavas. Where correlations
 941 are statistically significant, these are illustrated by bold lines and shaded regions showing the 95%
 942 confidence level of the correlation, both calculated using Isoplot [33]. Note that, despite nearly all
 943 samples have statistically indistinguishable $\mu^{142}\text{Nd}$ compositions, the strong variability of the
 944 abscissa variables (except for $\mu^{182}\text{W}$, panel e) means that the two-dimensional correlations are built
 945 on statistically independent points (i.e. their error ellipses do not statistically overlap). This is
 946 further evidenced by robust MSWD and probabilities of fit. For $\mu^{142}\text{Nd}$ vs. $^{206}\text{Pb}/^{204}\text{Pb}$ ratios (panel

947 c), a correlation is precluded by the very similar Pb isotopic compositions of FOZO- and EM-group
948 samples, which nevertheless have distinct $\mu^{142}\text{Nd}$ signatures. The qualitative senses of data trends
949 are outlined by dashed lines. For $\mu^{142}\text{Nd}$ versus Ce/Pb ratios (panel d), the uncertainty on Ce/Pb
950 ratios is calculated assuming 2% uncertainty for Ce and 5% uncertainty for Pb, which are typical
951 for bulk trace element analyses. This produces the minimum number of statistically distinct
952 correlation points between panels a, b, and d, with $n = 4$ in the case of panel d. Additionally, sample
953 FH-OM-3 is excluded from this correlation and we note that the Ce abundances for this sample
954 published in [37] and [28] disagree with each other by a factor of ~ 5 (Pb abundances were not
955 reported in [37]).

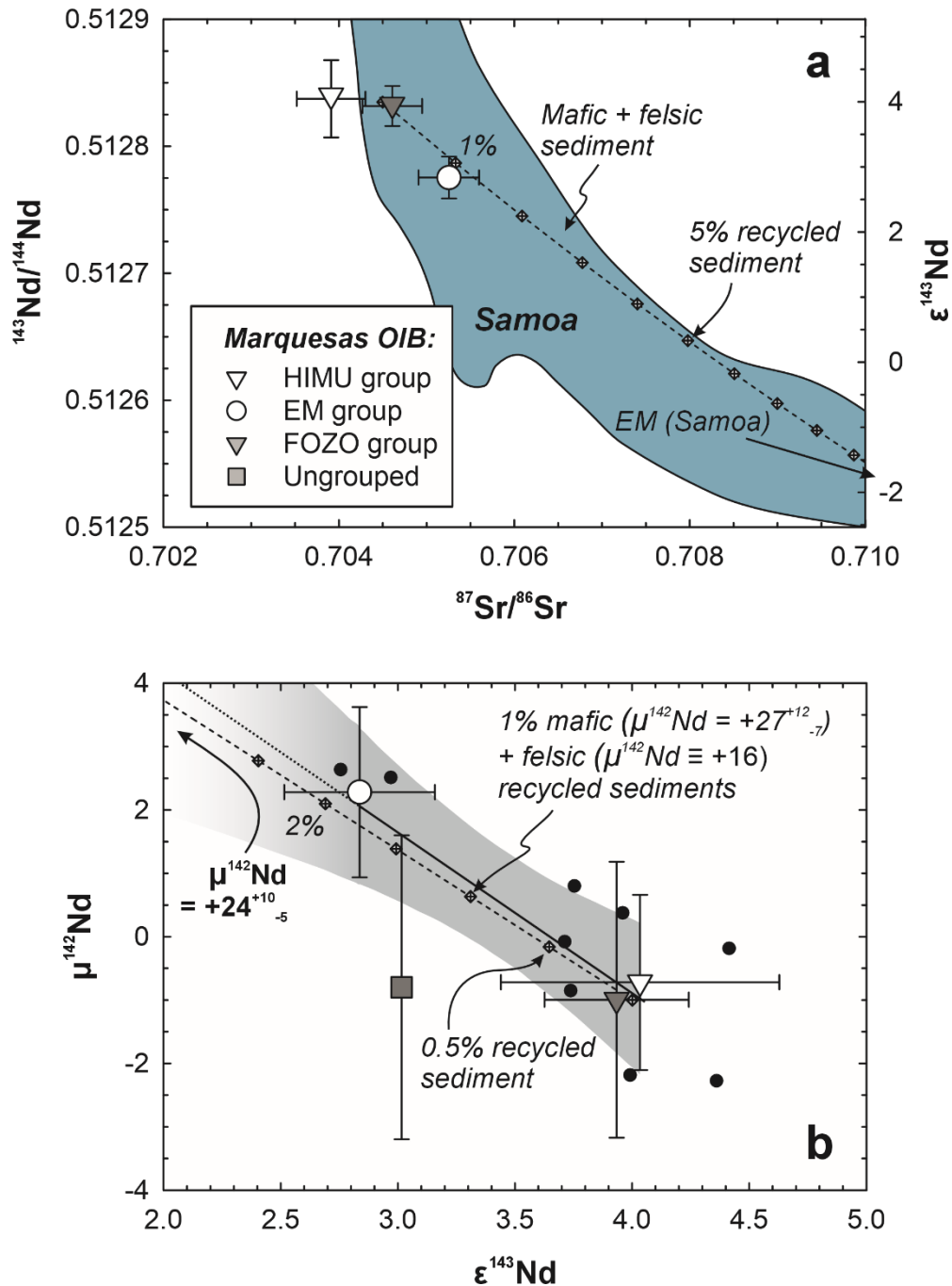
956



957

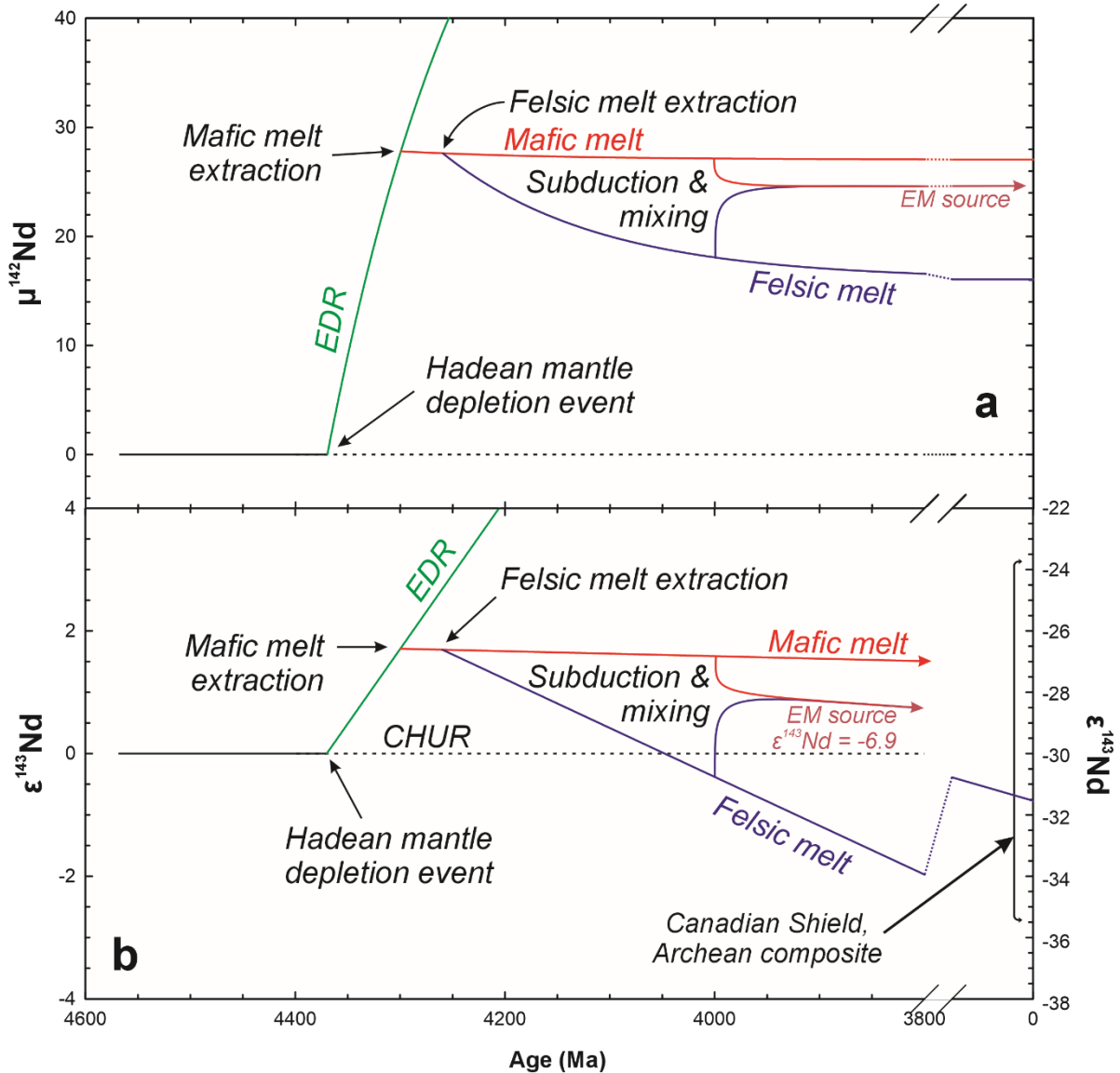
958 **Figure S2.** Long-lived radiogenic isotopic compositions of Marquesas samples in this study
 959 compared to literature data for Marquesas lavas [27, 56-58]. Best fit regressions for the Ua Huka
 960 and Fatu Hiva groups of [27] along with outlined regions encompassing all regression curves from
 961 [27] are shown for reference. Distinct trends for HIMU- and EM-group samples in panel c reflect
 962 the fact that EM and HIMU are not known to directly mix, but rather are only associated through
 963 a FOZO component (e.g., [101]). Illustrative mixing trends between a FOZO-like component and
 964 HIMU or EM through data for Marquesas OIB are shown. The trend of Marquesas EM-type lavas
 965 outside the field of Samoa implies that the two EM endmembers of these two hotspots must have
 966 distinct Sr and/or He abundances, but not necessarily that their EM endmember has a distinct He-
 967 Sr isotopic composition. Reference data for Samoa basalts is from the GEOROC database
 968 precompiled file (December 2023 version).

969



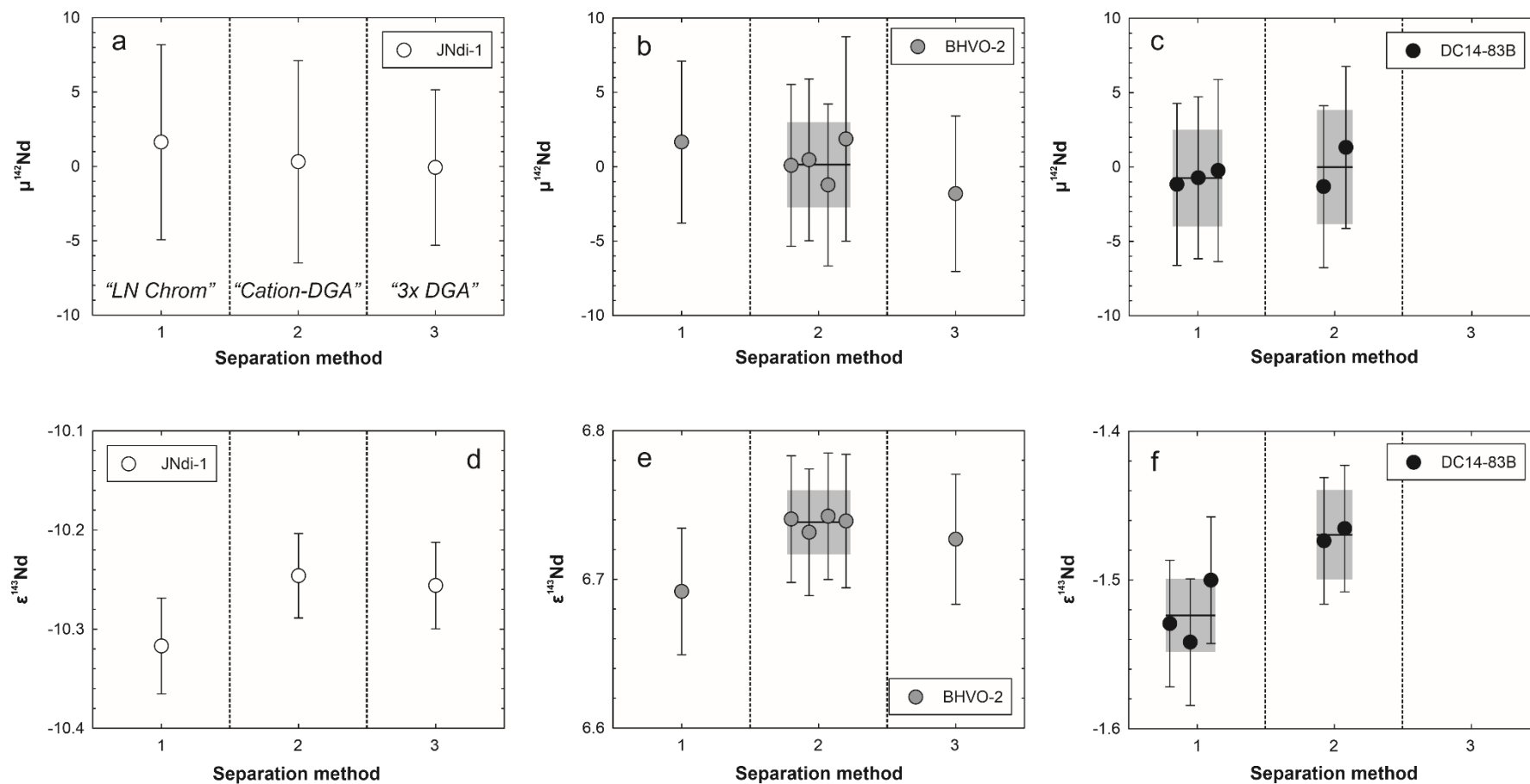
970

971 **Figure S3.** Refined model for the Sr-Nd isotopic compositions of Marquesas lavas calculating the
 972 compositions of mafic and felsic sedimentary members to the EM endmember (cf., **Figure 3**). The
 973 solid black line and gray shaded region represents the York-type linear regression and 95%
 974 confidence interval, respectively, of the $\mu^{142}\text{Nd}$ - $\epsilon^{143}\text{Nd}$ compositions of all samples [33]. The dotted
 975 black line and tapered gray shading represent an extrapolation of this regression. Large symbols
 976 and error bars show the per-group average and 95% confidence intervals, black circles show the
 977 per-sample measurements. The fraction of mixed EM component is noted by diamonds along the
 978 dashed mixing line. The compositional range of Samoa EM-type lavas is shown by the blue field
 979 in panel a with a reference to the assumed endmember Samoa Sr- ^{143}Nd isotopic composition from
 980 sample ALIA D115-21 [34].



982

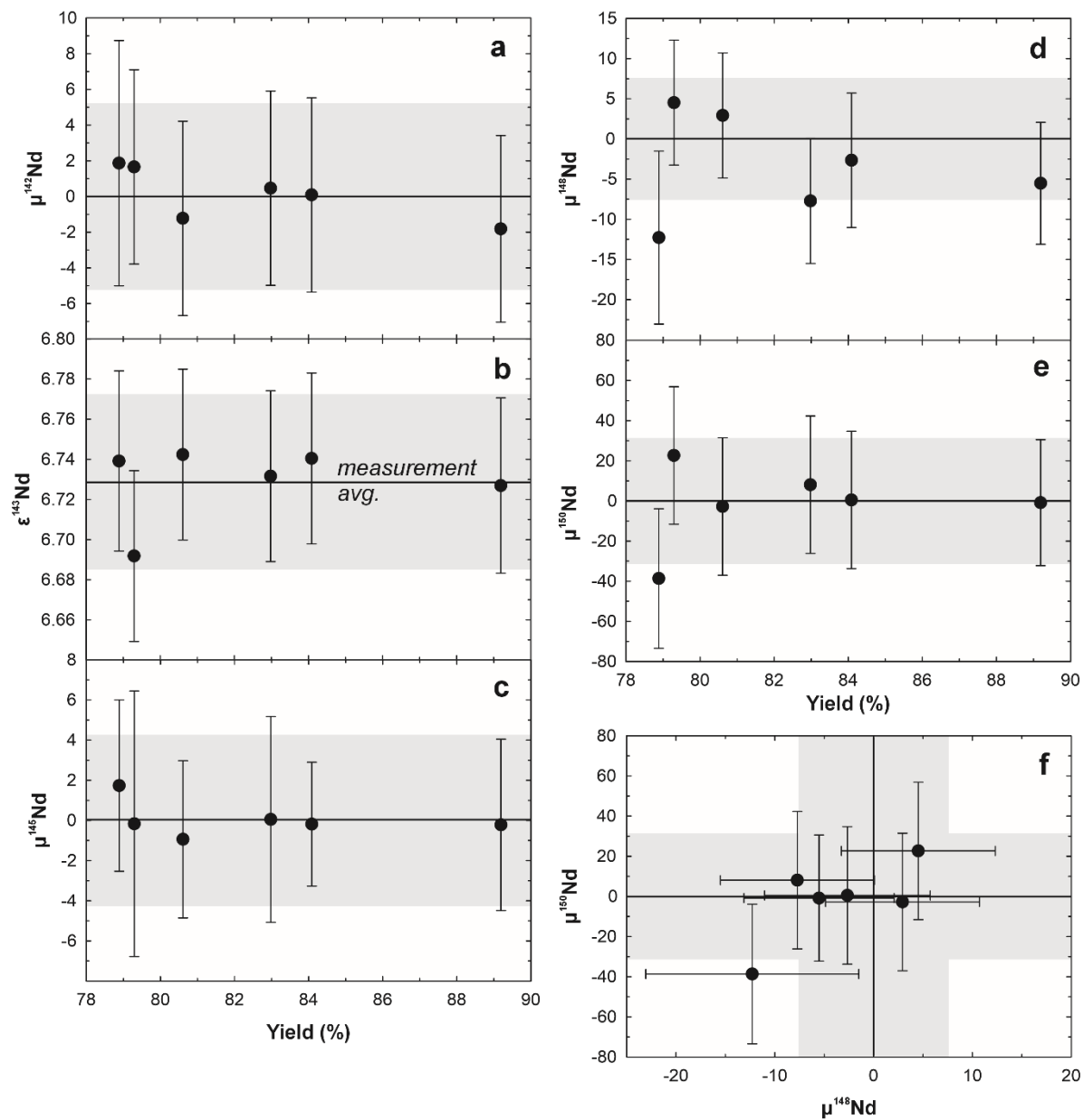
983 **Figure S4.** Assumed chronological evolution of the mafic and felsic components of the model
 984 shown in **Figure 3** and described in the main and supplementary texts. The model begins with a
 985 bulk Earth-like composition ($\mu^{142}\text{Nd} \equiv 0$) that is then differentiated during an event ca. 4.37 Ga
 986 ago, which is recorded in the Sm-Nd isotopic compositions of many global cratons [76], forming
 987 a depleted mantle domain. A mafic melt is then extracted from this depleted domain 4.26 Ga ago,
 988 and a felsic melt is produced from this mafic material at 4.1 Ga. For simplicity, it is assumed that
 989 the mafic and felsic materials reflecting the same chronological history are subducted together to
 990 form the Marquesas EM endmember, and possess a modern $\epsilon^{143}\text{Nd}$ composition identical to that of
 991 extreme Samoa sample ALIA D115-21 [39]. The range of Archean crust composites in panel b is
 992 from [77].



993

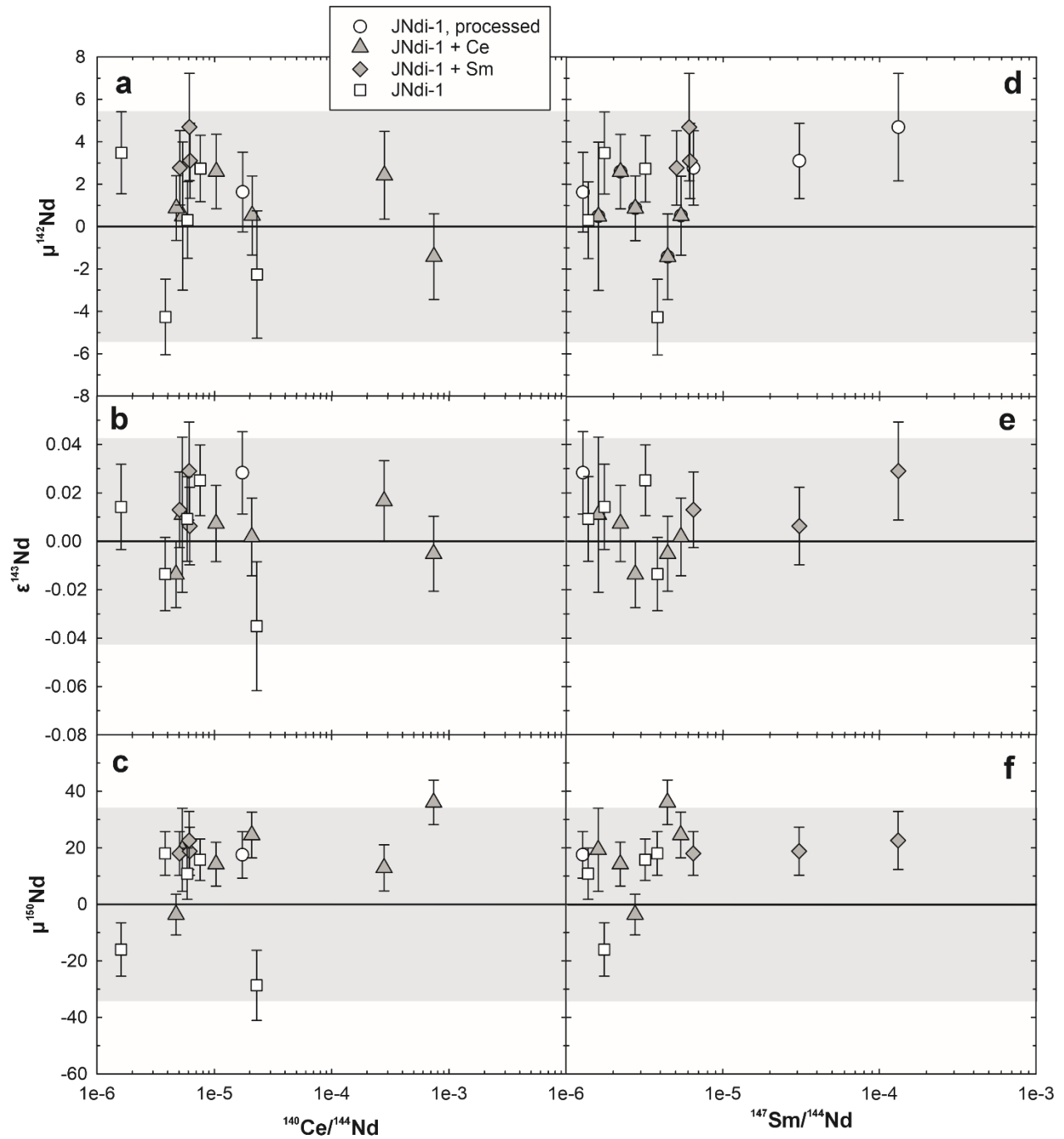
994

995 **Figure S5.** Comparison of Nd isotopic ratios measured in standard JNdi-1, United States Geological Survey reference material BHVO-2,
 996 and in-house reference material DC14-83B (lamprophyre, Deccan Traps) after processing through the three chemical separation methods
 997 described in the text.



998

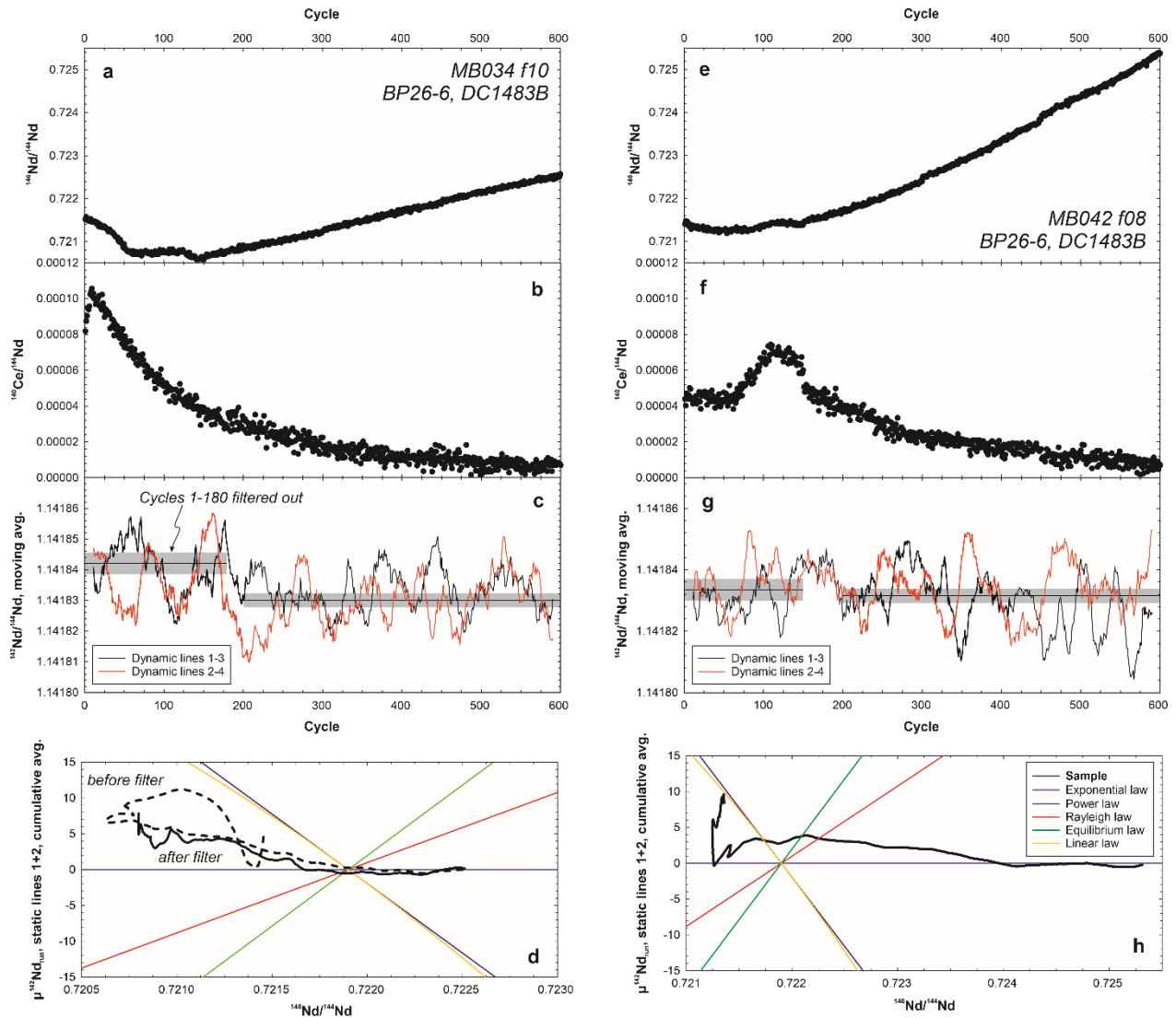
999 **Figure S6.** Comparison of yields for replicate aliquots of BHVO-2 versus Nd yield from separation
 1000 chemistry. In all cases, no systematic trend is observed, except potentially for one sample processed
 1001 using a long-aspect LN resin column (see text for details).



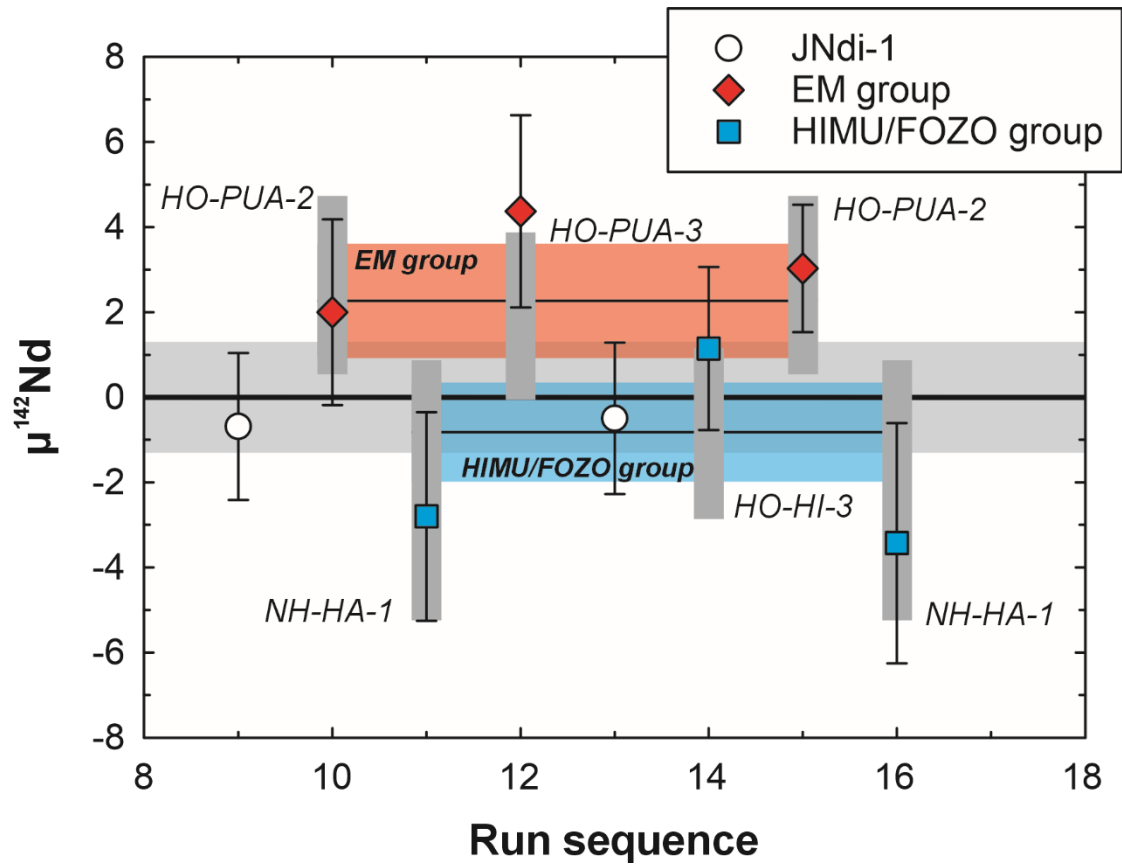
1002

1003 **Figure S7.** Neodymium isotopic compositions of JNdi-1 standards with and without added Ce or
 1004 Sm dopants. In all cases, no trends are observed outside of analytical uncertainty, and in all cases
 1005 measured sample $^{140}\text{Ce}/^{144}\text{Nd}$ and $^{147}\text{Sm}/^{144}\text{Nd}$ ratios were less than the maximum doped ratio
 1006 displayed in this figure. In this figure, error bars represent the 2σ standard error of each
 1007 measurement and the gray shaded region represents the medium-term analytical precision for each
 1008 isotope ratio.

1009

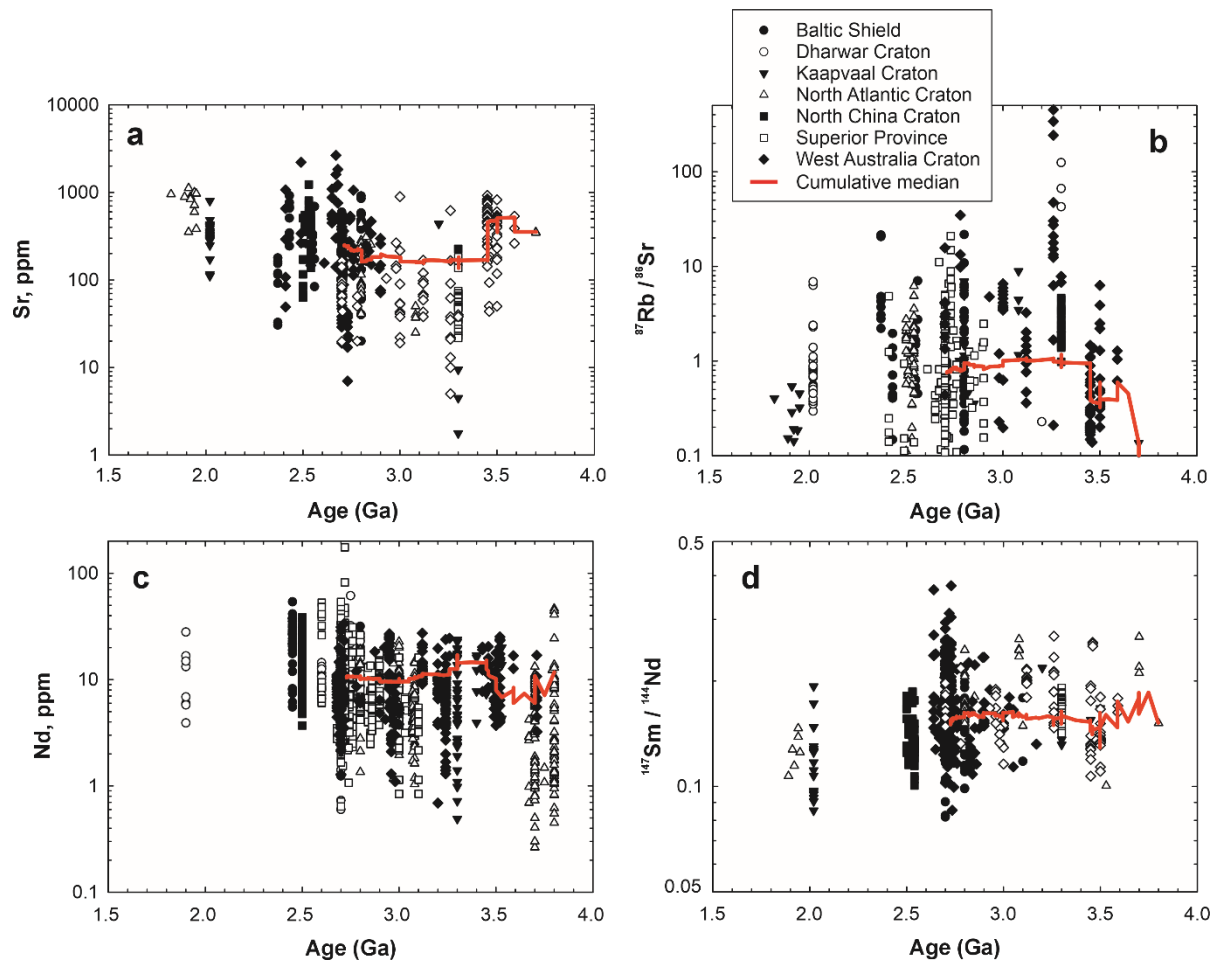


1010
 1011 **Figure S8.** Example of data filtering for two replicate measurements of the same digestion of in-
 1012 house reference material DC14-83B. The evolution of uncorrected $^{146}\text{Nd}/^{144}\text{Nd}$ ratios through the
 1013 run is non-linear for the first ca. 25% of each run, implying that the corrected isotopic data could
 1014 preserve mass-dependent isotopic effects, for example from domain mixing (e.g., [66]). In the first
 1015 case (panels a-d), this is evident from higher $^{142}\text{Nd}/^{144}\text{Nd}$ ratios measured in cycles 1-180 and from
 1016 possible non-exponential fractionation effects recorded in static $^{142}\text{Nd}/^{144}\text{Nd}$ ratios (panel d). These
 1017 measurement cycles were thus removed from the data correction. However, in the second case
 1018 (panels e-h) no effect on $^{142}\text{Nd}/^{144}\text{Nd}$ ratios (or any other Nd isotopic ratio) is observed, nor do
 1019 static $^{142}\text{Nd}/^{144}\text{Nd}$ ratios evolve in a pattern parallel to non-exponential fractionation (panel h), and
 1020 thus no data filtering is undertaken for this run.
 1021



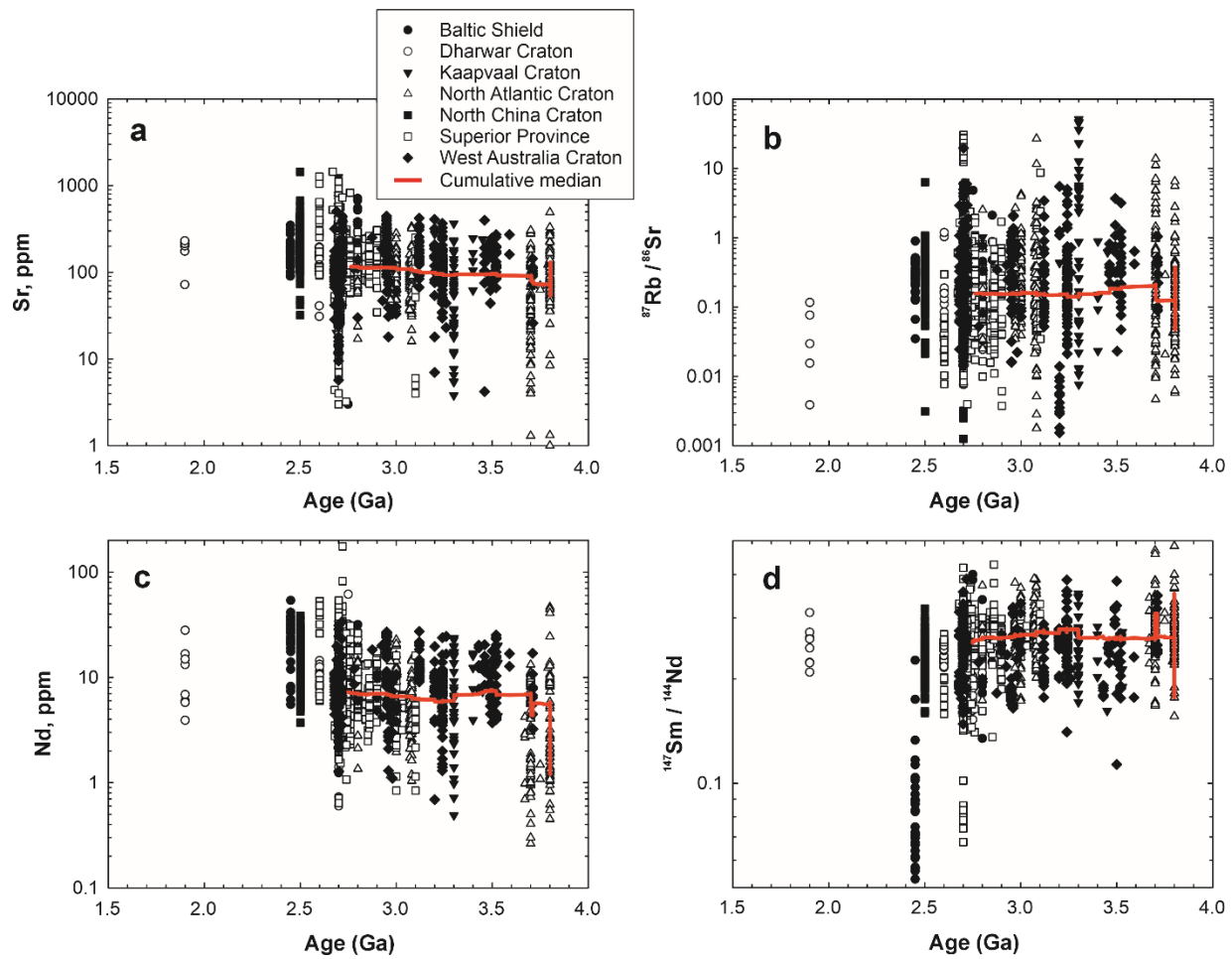
1022
 1023
 1024
 1025
 1026
 1027
 1028
 1029
 1030

Figure S9. Results of the sample 'challenge' described in the Supplementary Information. Samples are plotted in run order to emphasize the ability of the mass spectrometer to resolve the $\mu^{142}\text{Nd}$ compositions of compositionally distinct samples in a short time period. Error bars represent 2σ s.e.m., vertical dark gray shaded boxes represent the 95% confidence intervals of all runs for each sample, and the horizontal light gray shaded region represents the 2σ s.d. of all standards run in the same session.



1031
 1032 **Figure S10.** Abundances of Sr and Nd, Rb/Sr and Sm/Nd ratios for compiled felsic rocks from
 1033 global cratons. Cumulative medians are shown by thick red lines, demonstrating no significant
 1034 temporal change in the data across the Archean Era (4.0 to 2.5 Ga ago). Data assembled from the
 1035 precompiled files of GEOROC (version December 2023).

1036



1037

1038 **Figure S11.** Abundances of Sr and Nd, Rb/Sr and Sm/Nd ratios for compiled mafic rocks from
 1039 global cratons. Cumulative medians are shown by thick red lines, demonstrating no significant
 1040 temporal change in the data across the Archean Era (4.0 to 2.5 Ga ago). Data assembled from the
 1041 precompiled files of GEOROC (version December 2023).

1042

1043

References

- 1045 1. Foley, B.J., *The Role of Plate Tectonic–Climate Coupling and Exposed Land Area in the*
1046 *Development of Habitable Climates on Rocky Planets*. The Astrophysical Journal, 2015. **812**(1).
- 1047 2. Stern, R.J. and T. Gerya, *Subduction initiation in nature and models: A review*. Tectonophysics,
1048 2018. **746**: p. 173-198.
- 1049 3. Brown, M., T. Johnson, and N.J. Gardiner, *Plate Tectonics and the Archean Earth*. Annual Review
1050 of Earth and Planetary Sciences, 2020. **48**(1): p. 291-320.
- 1051 4. Martin, H., *Petrogenesis of Archean trondhjemites, tonalites, and granodiorites from eastern*
1052 *Finland: major and trace element geochemistry*. Journal of Petrology, 1987. **28**(5): p. 921-953.
- 1053 5. Wilde, S.A., J.W. Valley, W.H. Peck, and C.M. Graham, *Evidence from detrital zircons for the*
1054 *existence of continental crust and oceans on the Earth 4.4 Gyr ago*. Nature, 2001. **409**: p. 175-
1055 178.
- 1056 6. Turner, S., S. Wilde, G. Worner, B. Schaefer, and Y.J. Lai, *An andesitic source for Jack Hills*
1057 *zircon supports onset of plate tectonics in the Hadean*. Nat Commun, 2020. **11**(1): p. 1241.
- 1058 7. Guo, M. and J. Korenaga, *The combined Hf and Nd isotope evolution of the depleted mantle*
1059 *requires Hadean continental formation*. Science Advances, 2023. **9**.
- 1060 8. McCoy-West, A.J., P. Chowdhury, K.W. Burton, P. Sossi, G.M. Nowell, J.G. Fitton, A.C. Kerr,
1061 P.A. Cawood, and H.M. Williams, *Extensive crustal extraction in Earth's early history inferred*
1062 *from molybdenum isotopes*. Nature Geoscience, 2019. **12**(11): p. 946-951.
- 1063 9. Johnson, T.E., M. Brown, N.J. Gardiner, C.L. Kirkland, and R.H. Smithies, *Earth's first stable*
1064 *continents did not form by subduction*. Nature, 2017. **543**(7644): p. 239-242.
- 1065 10. Smithies, R.H., Y. Lu, T.E. Johnson, C.L. Kirkland, K.F. Cassidy, D.C. Champion, D.R. Mole, I.
1066 Zibra, K. Gessner, J. Sapkota, M.C. De Paoli, and M. Poujol, *No evidence for high-pressure*
1067 *melting of Earth's crust in the Archean*. Nat Commun, 2019. **10**(1): p. 5559.
- 1068 11. Wang, Q. and S.A. Wilde, *New constraints on the Hadean to Proterozoic history of the Jack Hills*
1069 *belt, Western Australia*. Gondwana Research, 2018. **55**: p. 74-91.
- 1070 12. Stern, R.J., *The Orosirian (1800–2050 Ma) plate tectonic episode: Key for reconstructing the*
1071 *Proterozoic tectonic record*. Geoscience Frontiers, 2023. **14**(3).
- 1072 13. Brown, M., T. Johnson, and C.J. Spencer, *Secular changes in metamorphism and metamorphic*
1073 *cooling rates track the evolving plate-tectonic regime on Earth*. Journal of the Geological Society,
1074 2022. **179**.
- 1075 14. Windley, B.F., T. Kusky, and A. Polat, *Onset of plate tectonics by the Eoarchean*. Precambrian
1076 Research, 2021. **352**.
- 1077 15. Copley, A. and O.M. Weller, *Modern-style continental tectonics since the early Archean*.
1078 Precambrian Research, 2024. **403**.
- 1079 16. Horan, M.F., R.W. Carlson, R.J. Walker, M. Jackson, M. Garçon, and M. Norman, *Tracking*
1080 *Hadean processes in modern basalts with 142-Neodymium*. Earth and Planetary Science Letters,
1081 2018. **484**: p. 184-191.
- 1082 17. Mundl-Petermeier, A., R.J. Walker, R.A. Fischer, V. Lekic, M.G. Jackson, and M.D. Kurz,
1083 *Anomalous 182W in high 3He/4He ocean island basalts: Fingerprints of Earth's core?*
1084 *Geochimica et Cosmochimica Acta*, 2020. **271**: p. 194-211.
- 1085 18. Williams, C.D. and S. Mukhopadhyay, *Capture of nebular gases during Earth's accretion is*
1086 *preserved in deep-mantle neon*. Nature, 2019. **565**(7737): p. 78-81.
- 1087 19. O'Neil, J., R.W. Carlson, D. Francis, and R.K. Stevenson, *Neodymium-142 Evidence for Hadean*
1088 *Mafic Crust*. Science, 2008. **321**: p. 1828-1831.
- 1089 20. Jackson, M.G., T.W. Becker, and J.G. Konter, *Evidence for a deep mantle source for EM and*
1090 *HIMU domains from integrated geochemical and geophysical constraints*. Earth and Planetary
1091 Science Letters, 2018. **484**: p. 154-167.
- 1092 21. Gülcher, A.J.P., M.D. Ballmer, and P.J. Tackley, *Coupled dynamics and evolution of primordial*
1093 *and recycled heterogeneity in Earth's lower mantle*. Solid Earth, 2021. **12**(9): p. 2087-2107.

- 1094 22. Koppers, A.A.P., T.W. Becker, M.G. Jackson, K. Konrad, R.D. Müller, B. Romanowicz, B.
1095 Steinberger, and J.M. Whittaker, *Mantle plumes and their role in Earth processes*. Nature Reviews
1096 Earth & Environment, 2020. **2**: p. 382-401.
- 1097 23. Jones, T.D., R.R. Maguire, P.E. van Keken, J. Ritsema, and P. Koelemeijer, *Subducted oceanic
1098 crust as the origin of seismically slow lower-mantle structures*. Progress in Earth and Planetary
1099 Science, 2020. **7**(1).
- 1100 24. Jackson, M.G., T.W. Becker, and B. Steinberger, *Spatial Characteristics of Recycled and
1101 Primordial Reservoirs in the Deep Mantle*. Geochemistry, Geophysics, Geosystems, 2021. **22**(3).
- 1102 25. Giuliani, A., M.G. Jackson, A. Fitzpayne, and H. Dalton, *Remnants of early Earth differentiation
1103 in the deepest mantle-derived lavas*. Proc Natl Acad Sci U S A, 2021. **118**(1).
- 1104 26. Chauvel, C., A.W. Hofmann, and P. Vidal, *HIMU-EM: The French Polynesian connection*. Earth
1105 and Planetary Science Letters, 1992. **110**: p. 99-119.
- 1106 27. Chauvel, C., R.C. Maury, S. Blais, E. Lewin, H. Guillou, G. Guille, P. Rossi, and M.-A. Gutscher,
1107 *The size of plume heterogeneities constrained by Marquesas isotopic stripes*. Geochemistry,
1108 Geophysics, Geosystems, 2012. **13**(7): p. n/a-n/a.
- 1109 28. Nicklas, R.W., J.M.D. Day, T.D. Jones, and P.R. Castillo, *Evidence for a primitive deep mantle
1110 component in the source of Marquesas Islands Lavas from Os isotope and highly siderophile
1111 element abundance systematics*. Geochimica et Cosmochimica Acta, 2022. **329**: p. 51-69.
- 1112 29. Stracke, A., *Earth's heterogeneous mantle: A product of convection-driven interaction between
1113 crust and mantle*. Chemical Geology, 2012. **330-331**: p. 274-299.
- 1114 30. Herret, M.T., B.J. Peters, D. Kim, P.R. Castillo, and A. Mundl-Petermeier, *Decoupling of short-
1115 lived radiogenic and helium isotopes in the Marquesas hotspot*. Chemical Geology, 2023. **640**.
- 1116 31. Friedman, A.M., J. Milsted, D. Metta, D. Henderson, J. Lerner, A.L. Harkness, and D.J. Rokop,
1117 *Alpha decay half lives of ^{148}Gd , ^{150}Gd , and ^{146}Sm* . Radiochimica Acta, 1966. **5**(4): p. 192-194.
- 1118 32. Tanaka, T., S. Togashi, H. Kamioka, H. Amakawa, H. Kagami, T. Hamamoto, M. Zuhara, Y.
1119 Orihashi, S. Yoneda, H. Shimizu, T. Kunimaru, K. Takahashi, T. Zanagi, T. Nakano, H. Fujimaki,
1120 R. Shinjo, Y. Asahara, M. Tanimizu, and C. Dragusanu, *JNdi-1: a neodymium isotopic reference in
1121 consistency with LaJolla neodymium*. Chemical Geology, 2000. **168**: p. 279-281.
- 1122 33. Ludwig, K.R., *Isoplot 3.00: A geochronological toolkit for Microsoft Excel*. 2003, Berkeley
1123 Geochronology Center. p. 1-70.
- 1124 34. Jackson, M.G., S.R. Hart, A.A. Koppers, H. Staudigel, J. Konter, J. Blusztajn, M. Kurz, and J.A.
1125 Russell, *The return of subducted continental crust in Samoan lavas*. Nature, 2007. **448**(7154): p.
1126 684-7.
- 1127 35. O'Neil, J. and R.W. Carlson, *Building Archean cratons from Hadean mafic crust*. Science, 2017.
1128 **355**: p. 1199-1202.
- 1129 36. Willbold, M. and A. Stracke, *Formation of enriched mantle components by recycling of upper and
1130 lower continental crust*. Chemical Geology, 2010. **276**(3-4): p. 188-197.
- 1131 37. Castillo, P.R., P. Scarsi, and H. Craig, *He, Sr, Nd, and Pb isotopic constraints on the origin of the
1132 Marquesas and other linear volcanic chains*. Chemical Geology, 2007. **240**(3-4): p. 205-221.
- 1133 38. Hanyu, T. and I. Kaneoka, *The uniform and low $^3\text{He}/^4\text{He}$ ratios of HIMU basalts as evidence for
1134 their origin as recycled materials*. Nature, 2007. **390**: p. 273-276.
- 1135 39. Jackson, M.G., J. Blichert-Toft, S.A. Halldorsson, A. Mundl-Petermeier, M. Bizimis, M.D. Kurz,
1136 A.A. Price, S. Harethardottir, L.N. Willhite, K. Breddam, T.W. Becker, and R.A. Fischer, *Ancient
1137 helium and tungsten isotopic signatures preserved in mantle domains least modified by crustal
1138 recycling*. Proc Natl Acad Sci U S A, 2020. **117**(49): p. 30993-31001.
- 1139 40. Bennett, V.C., A.D. Brandon, and A.P. Nutman, *Coupled ^{142}Nd - ^{143}Nd Isotopic Evidence for
1140 Hadean Mantle Dynamics*. Science, 2007. **318**: p. 1907-1910.
- 1141 41. O'Neil, J., H. Rizo, M. Boyet, R.W. Carlson, and M.T. Rosing, *Geochemistry and Nd isotopic
1142 characteristics of Earth's Hadean mantle and primitive crust*. Earth and Planetary Science Letters,
1143 2016. **442**: p. 194-205.
- 1144 42. Boyet, M. and R. Carlson, *A new geochemical model for the Earth's mantle inferred from ^{146}Sm -
1145 ^{142}Nd systematics*. Earth and Planetary Science Letters, 2006. **250**(1-2): p. 254-268.

- 1146 43. Wasilewski, B., J. O'Neil, and H. Rizo, *Archean crustal evolution of the Saglek-Hebron Complex,*
1147 *Northern Labrador; revealed from coupled 147–146Sm-143–142Nd systematics.* Earth and
1148 Planetary Science Letters, 2022. **594**.
- 1149 44. Hyung, E. and S.B. Jacobsen, *The (142)Nd/(144)Nd variations in mantle-derived rocks provide*
1150 *constraints on the stirring rate of the mantle from the Hadean to the present.* Proc Natl Acad Sci
1151 U S A, 2020. **117**(26): p. 14738-14744.
- 1152 45. Rizo, H., M. Boyet, J. Blichert-Toft, J. O'Neil, M.T. Rosing, and J.L. Paquette, *The elusive*
1153 *Hadean enriched reservoir revealed by 142Nd deficits in Isua Archean rocks.* Nature, 2012.
1154 **491**(7422): p. 96-100.
- 1155 46. Nebel, O., F.A. Capitanio, J.F. Moyen, R.F. Weinberg, F. Clos, Y.J. Nebel-Jacobsen, and P.A.
1156 Cawood, *When crust comes of age: on the chemical evolution of Archean, felsic continental crust*
1157 *by crustal drip tectonics.* Philos Trans A Math Phys Eng Sci, 2018. **376**(2132).
- 1158 47. Klein, B.Z., O. Jagoutz, and M.D. Behn, *Archean crustal compositions promote full mantle*
1159 *convection.* Earth and Planetary Science Letters, 2017. **474**: p. 516-526.
- 1160 48. Konhauser, K.O., N.J. Planavsky, D.S. Hardisty, L.J. Robbins, T.J. Warchola, R. Haugaard, S.V.
1161 Lalonde, C.A. Partin, P.B.H. Oonk, H. Tsikos, T.W. Lyons, A. Bekker, and C.M. Johnson, *Iron*
1162 *formations: A global record of Neoproterozoic to Palaeoproterozoic environmental history.* Earth-
1163 Science Reviews, 2017. **172**: p. 140-177.
- 1164 49. Agić, H., M. Moczyłowska, and L. Yin, *Diversity of organic-walled microfossils from the early*
1165 *Mesoproterozoic Ruyang Group, North China Craton – A window into the early eukaryote*
1166 *evolution.* Precambrian Research, 2017. **297**: p. 101-130.
- 1167 50. Yin, A., *An episodic slab-rollback model for the origin of the Tharsis rise on Mars: Implications*
1168 *for initiation of local plate subduction and final unification of a kinematically linked global plate-*
1169 *tectonic network on Earth.* Lithosphere, 2012. **4**(6): p. 553-593.
- 1170 51. Davaille, A., S.E. Smrekar, and S. Tomlinson, *Experimental and observational evidence for*
1171 *plume-induced subduction on Venus.* Nature Geoscience, 2017. **10**(5): p. 349-355.
- 1172 52. Bouvier, A., J.D. Vervoort, and P.J. Patchett, *The Lu–Hf and Sm–Nd isotopic composition of*
1173 *CHUR: Constraints from unequilibrated chondrites and implications for the bulk composition of*
1174 *terrestrial planets.* Earth and Planetary Science Letters, 2008. **273**(1-2): p. 48-57.
- 1175 53. Graham, D.W., *Noble Gas Isotope Geochemistry of Mid-Ocean Ridge and Ocean Island Basalts:*
1176 *Characterization of Mantle Source Reservoirs.* Reviews in Mineralogy and Geochemistry, 2002.
1177 **47**(1): p. 247-317.
- 1178 54. Duncan, R.A. and I. McDougall, *Migration of volcanism with time in the Marquesas Islands,*
1179 *French Polynesia.* Earth and Planetary Science Letters, 1974. **21**: p. 414-420.
- 1180 55. Kim, D., B. Ménard, D. Baron, and M. Taghizadeh-Popp, *Sequencing seismograms: A panoptic*
1181 *view of scattering in the core-mantle boundary region.* Science, 2020. **368**: p. 1223-1228.
- 1182 56. Dupuy, C., P. Vidal, H.G. Barszczus, and C. Chauvel, *Origin of basalts from the Marquesas*
1183 *Archipelago (south central Pacific Ocean): isotope and trace element constraints.* Earth and
1184 Planetary Science Letters, 1987. **82**: p. 145-152.
- 1185 57. Woodhead, J.D., *Temporal geochemical evolution in oceanic intra-plate volcanics: a case study*
1186 *from the Marquesas (French Polynesia) and comparison with other hotspots.* Contributions to
1187 Mineralogy and Petrology, 1992. **111**: p. 458-467.
- 1188 58. Desonie, D.L., R.A. Duncan, and J.H. Natland, *Temporal and geochemical variability of volcanic*
1189 *products of the Marquesas Hotspot.* Journal of Geophysical Research: Solid Earth, 1993. **98**(B10):
1190 p. 17649-17665.
- 1191 59. Jackson, M., M. Kurz, S. Hart, and R. Workman, *New Samoan lavas from Ofu Island reveal a*
1192 *hemispherically heterogeneous high 3He/4He mantle.* Earth and Planetary Science Letters, 2007.
1193 **264**(3-4): p. 360-374.
- 1194 60. Woodhead, J.D., *Extreme HIMU in an oceanic setting: the geochemistry of Mangaia Island*
1195 *(Polynesia), and temporal evolution of the Cook-Austral hotspot.* Journal of Volcanology and
1196 Geothermal Research, 1996. **72**: p. 1-19.

- 1197 61. Garçon, M., M. Boyet, R.W. Carlson, M.F. Horan, D. Auclair, and T.D. Mock, *Factors influencing*
1198 *the precision and accuracy of Nd isotope measurements by thermal ionization mass spectrometry.*
1199 *Chemical Geology*, 2018. **476**: p. 493-514.
- 1200 62. Chu, Z.-Y., M.-J. Wang, C.-F. Li, Y.-H. Yang, J.-J. Xu, W. Wang, and J.-H. Guo, *Separation of Nd*
1201 *from geological samples by a single TODGA resin column for high precision Nd isotope analysis*
1202 *as NdO⁺ by TIMS.* *Journal of Analytical Atomic Spectrometry*, 2019. **34**(10): p. 2053-2060.
- 1203 63. Wang, D. and R.W. Carlson, *Tandem-column extraction chromatography for Nd separation:*
1204 *minimizing mass-independent isotope fractionation for ultrahigh-precision Nd isotope-ratio*
1205 *analysis.* *Journal of Analytical Atomic Spectrometry*, 2022. **37**(1): p. 185-193.
- 1206 64. Jochum, K.P., U. Nohl, K. Herwig, E. Lammel, B. Stoll, and A.W. Hofmann, *GeoReM: A New*
1207 *Geochemical Database for Reference Materials and Isotopic Standards.* *Geostandards and*
1208 *Geoanalytical Research*, 2005. **29**(3): p. 333-338.
- 1209 65. Saji, N.S., D. Wielandt, C. Paton, and M. Bizzarro, *Ultra-high-precision Nd-isotope*
1210 *measurements of geological materials by MC-ICPMS.* *J Anal At Spectrom*, 2016. **31**(7): p. 1490-
1211 1504.
- 1212 66. Andreasen, R. and M. Sharma, *Fractionation and mixing in a thermal ionization mass*
1213 *spectrometer source: Implications and limitations for high-precision Nd isotope analyses.*
1214 *International Journal of Mass Spectrometry*, 2009. **285**(1-2): p. 49-57.
- 1215 67. Peters, B.J., R.W. Carlson, J.M.D. Day, and M.F. Horan, *Hadean silicate differentiation preserved*
1216 *by anomalous (142)Nd/(144)Nd ratios in the Reunion hotspot source.* *Nature*, 2018. **555**(7694): p.
1217 89-93.
- 1218 68. Peters, B.J., A. Mundl-Petermeier, R.W. Carlson, R.J. Walker, and J.M.D. Day, *Combined*
1219 *Lithophile-Siderophile Isotopic Constraints on Hadean Processes Preserved in Ocean Island*
1220 *Basalt Sources.* *Geochemistry, Geophysics, Geosystems*, 2021. **22**(3).
- 1221 69. Peters, B.J., J.M.D. Day, and L.A. Taylor, *Early mantle heterogeneities in the Réunion hotspot*
1222 *source inferred from highly siderophile elements in cumulate xenoliths.* *Earth and Planetary*
1223 *Science Letters*, 2016. **448**: p. 150-160.
- 1224 70. Zhang, Y. and Y. Liu, *How to produce isotope anomalies in mantle by using extremely small*
1225 *isotope fractionations: A process-driven amplification effect?* *Geochimica et Cosmochimica Acta*,
1226 2020. **291**: p. 19-49.
- 1227 71. Baker, J., D. Peate, T. Waight, and C. Meyzen, *Pb isotopic analysis of standards and samples*
1228 *using a 207Pb–204Pb double spike and thallium to correct for mass bias with a double-focusing*
1229 *MC-ICP-MS.* *Chemical Geology*, 2004. **211**(3-4): p. 275-303.
- 1230 72. McDonough, W.F. and S.-s. Sun, *The composition of the Earth.* *Chemical Geology*, 1995. **120**: p.
1231 223-253.
- 1232 73. Rudnick, R.L. and S. Gao, *Composition of the continental crust*, in *Treatise on Geochemistry*,
1233 H.D. Holland and K.K. Turekian, Editors. 2003, Elsevier. p. 1-64.
- 1234 74. Plank, T., *The Chemical Composition of Subducting Sediments*, in *Treatise on Geochemistry*.
1235 2014. p. 607-629.
- 1236 75. Rizo, H., M. Boyet, J. Blichert-Toft, and M.T. Rosing, *Early mantle dynamics inferred from*
1237 *142Nd variations in Archean rocks from southwest Greenland.* *Earth and Planetary Science*
1238 *Letters*, 2013. **377-378**: p. 324-335.
- 1239 76. Morino, P., G. Caro, L. Reisberg, and A. Schumacher, *Chemical stratification in the post-magma*
1240 *ocean Earth inferred from coupled 146,147Sm–142,143Nd systematics in ultramafic rocks of the*
1241 *Saglek block (3.25–3.9 Ga; northern Labrador, Canada).* *Earth and Planetary Science Letters*,
1242 2017. **463**: p. 136-150.
- 1243 77. McCulloch, M.T. and G.J. Wasserburg, *Sm-Nd and Rb-Sr Chronology of Continental Crust*
1244 *Formation.* *Science*, 1978. **200**: p. 1003-1011.
- 1245 78. Garapić, G., M.G. Jackson, E.H. Hauri, S.R. Hart, K.A. Farley, J.S. Blusztajn, and J.D. Woodhead,
1246 *A radiogenic isotopic (He-Sr-Nd-Pb-Os) study of lavas from the Pitcairn hotspot: Implications for*
1247 *the origin of EM-1 (enriched mantle 1).* *Lithos*, 2015. **228-229**: p. 1-11.

- 1248 79. Millot, R., C.-J. Allègre, J. Gaillardet, and S. Roy, *Lead isotopic systematics of major river*
1249 *sediments: a new estimate of the Pb isotopic composition of the Upper Continental Crust.*
1250 *Chemical Geology*, 2004. **203**(1-2): p. 75-90.
- 1251 80. Andreassen, R., M. Sharma, K.V. Subbarao, and S.G. Viladkar, *Where on Earth is the enriched*
1252 *Hadean reservoir?* *Earth and Planetary Science Letters*, 2008. **266**(1-2): p. 14-28.
- 1253 81. Archer, G.J., G.A. Brennecke, P. Gleißner, A. Stracke, H. Becker, and T. Kleine, *Lack of late-*
1254 *accreted material as the origin of ^{182}W excesses in the Archean mantle: Evidence from the*
1255 *Pilbara Craton, Western Australia.* *Earth and Planetary Science Letters*, 2019. **528**.
- 1256 82. Caro, G., B. Bourdon, J.-L. Birck, and S. Moorbath, *High-precision $^{142}\text{Nd}/^{144}\text{Nd}$ measurements*
1257 *in terrestrial rocks: Constraints on the early differentiation of the Earth's mantle.* *Geochimica et*
1258 *Cosmochimica Acta*, 2006. **70**(1): p. 164-191.
- 1259 83. Caro, G., P. Morino, S.J. Mojzsis, N.L. Cates, and W. Bleeker, *Sluggish Hadean geodynamics:*
1260 *Evidence from coupled ^{146}Sm – ^{142}Nd systematics in Eoarchean supracrustal rocks of*
1261 *the Inukjuak domain (Québec).* *Earth and Planetary Science Letters*, 2017. **457**: p. 23-37.
- 1262 84. Cipriani, A., E. Bonatti, and R.W. Carlson, *Nonchondritic ^{142}Nd in suboceanic mantle peridotites.*
1263 *Geochemistry, Geophysics, Geosystems*, 2011. **12**(3): p. n/a-n/a.
- 1264 85. de Leeuw, G.A.M., R.M. Ellam, F.M. Stuart, and R.W. Carlson, *$^{142}\text{Nd}/^{144}\text{Nd}$ inferences on the*
1265 *nature and origin of the source of high $^3\text{He}/^4\text{He}$ magmas.* *Earth and Planetary Science Letters*,
1266 2017. **472**: p. 62-68.
- 1267 86. O'Neill, C., V. Debaille, and W. Griffin, *Deep earth recycling in the Hadean and constraints on*
1268 *surface tectonics.* *American Journal of Science*, 2013. **313**(9): p. 912-932.
- 1269 87. Jackson, M.G. and R.W. Carlson, *Homogeneous superchondritic $^{142}\text{Nd}/^{144}\text{Nd}$ in the mid-ocean*
1270 *ridge basalt and ocean island basalt mantle.* *Geochemistry, Geophysics, Geosystems*, 2012.
1271 **13**(6): p. n/a-n/a.
- 1272 88. Maltese, A., G. Caro, O.P. Pandey, D. Upadhyay, and K. Mezger, *Direct evidence for crust-mantle*
1273 *differentiation in the late Hadean.* *Communications Earth & Environment*, 2022. **3**(1).
- 1274 89. Mei, Q.-F., J.-H. Yang, C.-F. Li, X.-C. Wang, J. Konnunaho, Y.-D. Wu, H. Zhong, Y.-G. Xu, and
1275 H. Wang, *Modern ocean island basalt-like ^{182}W signature in Paleoarchean mafic rocks:*
1276 *Implications for the generation, preservation, and destruction of early mantle heterogeneities.*
1277 *Geology*, 2023. **51**(10): p. 919-923.
- 1278 90. Murphy, D.T., A.D. Brandon, V. Debaille, R. Burgess, and C. Ballentine, *In search of a hidden*
1279 *long-term isolated sub-chondritic $^{142}\text{Nd}/^{144}\text{Nd}$ reservoir in the deep mantle: Implications for the*
1280 *Nd isotope systematics of the Earth.* *Geochimica et Cosmochimica Acta*, 2010. **74**(2): p. 738-750.
- 1281 91. Murphy, D., H. Rizo, J. O'Neil, R. Hepple, D. Wiemer, A. Kemp, and J. Vervoort, *Combined Sm-*
1282 *Nd, Lu-Hf, and ^{142}Nd study of Paleoarchean basalts from the East Pilbara Terrane, Western*
1283 *Australia.* *Chemical Geology*, 2021. **578**.
- 1284 92. Puchtel, I.S., J. Blichert-Toft, M. Touboul, M.F. Horan, and R.J. Walker, *The coupled ^{182}W - ^{142}Nd*
1285 *record of early terrestrial mantle differentiation.* *Geochemistry, Geophysics, Geosystems*, 2016.
1286 **17**(6): p. 2168-2193.
- 1287 93. Reimink, J.R., J.H.F.L. Davies, A.M. Bauer, and T. Chacko, *A comparison between zircons from*
1288 *the Acasta Gneiss Complex and the Jack Hills region.* *Earth and Planetary Science Letters*, 2020.
1289 **531**.
- 1290 94. Reimink, J.R., T. Chacko, R.W. Carlson, S.B. Shirey, J. Liu, R.A. Stern, A.M. Bauer, D.G.
1291 Pearson, and L.M. Heaman, *Petrogenesis and tectonics of the Acasta Gneiss Complex derived*
1292 *from integrated petrology and ^{142}Nd and ^{182}W extinct nuclide-geochemistry.* *Earth and Planetary*
1293 *Science Letters*, 2018. **494**: p. 12-22.
- 1294 95. Rizo, H., M. Boyet, J. Blichert-Toft, and M. Rosing, *Combined Nd and Hf isotope evidence for*
1295 *deep-seated source of Isua lavas.* *Earth and Planetary Science Letters*, 2011. **312**(3-4): p. 267-279.
- 1296 96. Roth, A.S.G., E.E. Scherer, C. Maden, K. Mezger, and B. Bourdon, *Revisiting the ^{142}Nd deficits*
1297 *in the 1.48 Ga Khariar alkaline rocks, India.* *Chemical Geology*, 2014. **386**: p. 238-248.

- 1298 97. Roth, A.S.G., B. Bourdon, S.J. Mojzsis, M. Touboul, P. Sprung, M. Guitreau, and J. Blichert-Toft,
1299 *Inherited ^{142}Nd anomalies in Eoarchean protoliths*. Earth and Planetary Science Letters, 2013.
1300 **361**: p. 50-57.
- 1301 98. Saji, N.S., K. Larsen, D. Wielandt, M. Schiller, M.M. Costa, M.J. Whitehouse, M.T. Rosing, and
1302 M. Bizzarro, *Hadean geodynamics inferred from time-varying $(^{142}\text{Nd}/(^{144}\text{Nd}))$ in the early Earth*
1303 *rock record*. Geochem Perspect Lett, 2018. **7**: p. 43-48.
- 1304 99. Schneider, K.P., J.E. Hoffmann, M. Boyet, C. Münker, and A. Kröner, *Coexistence of enriched*
1305 *and modern-like ^{142}Nd signatures in Archean igneous rocks of the eastern Kaapvaal Craton,*
1306 *southern Africa*. Earth and Planetary Science Letters, 2018. **487**: p. 54-66.
- 1307 100. Wainwright, A.N., F. El Atrassi, V. Debaille, and N. Mattielli, *Geochemistry and petrogenesis of*
1308 *Archean mafic rocks from the Amsaga area, West African craton, Mauritania*. Precambrian
1309 Research, 2019. **324**: p. 208-219.
- 1310 101. Stracke, A., A.W. Hofmann, and S.R. Hart, *FOZO, HIMU, and the rest of the mantle zoo*.
1311 *Geochemistry, Geophysics, Geosystems*, 2005. **6**(5).